

Random layers for quantum optimal control with exponential expressivity

Marco Dall’Ara,¹ Martin Koppenhöfer,¹ Florentin Reiter,¹
Thomas Wellens,¹ Simone Montangero,^{2,3,4} and Walter Hahn^{1,*}

¹Fraunhofer Institute for Applied Solid State Physics IAF, Tullastr. 72, 79108 Freiburg, Germany

²Dipartimento di Fisica e Astronomia “G. Galilei”, Università di Padova, I-35131 Padova, Italy

³Padua Quantum Technologies Research Center, Università degli Studi di Padova, I-35131 Padova, Italy

⁴Istituto Nazionale di Fisica Nucleare (INFN), Sezione di Padova, I-35131 Padova, Italy

A long-standing challenge in quantum optimal control is finding an optimal pulse structure that leads to an efficient exploration of the unitary space with a minimal number of optimization parameters. We solve this challenge by constructing parametrized pulse sequences from random constant-amplitude pulses grouped in layers with one optimization parameter per layer. We show that, when increasing the number of pulses, the resulting random unitaries converge exponentially fast to the uniform Haar-random ensemble. Grouping the pulses into layers allows to lower the total number of optimization parameters. We focus on two random-layer (RALLY) methods: In RALLY_T, time durations of the layers are optimized while the pulse amplitudes are randomly chosen beforehand, possibly even from a few discrete values. RALLY_A optimizes a joint scaling factor of the random pulse amplitudes in each layer. We numerically validate the two methods by applying them to problems of unitary synthesis, ground-state preparation and state transfer in different quantum systems. For all problems considered, both methods approach an information-theoretic lower bound on the number of optimization parameters and outperform other commonly used algorithms. In gradient-free optimization, the RALLY methods are orders of magnitude more accurate with fewer figure-of-merit evaluations. The RALLY methods are also applicable for enhanced quantum machine learning and variational quantum algorithms.

I. INTRODUCTION

Precise and fast control of quantum systems is essential for many problems in quantum science and technology. Quantum optimal control theory provides methods to achieve such control by designing pulse sequences that, for example, steer quantum systems to target states or induce target dynamics [1–3]. These pulse sequences are obtained by optimizing a suitable figure of merit either directly on a quantum device (closed-loop) or using a numerical model of the quantum system (open-loop) [4–21].

With increasing size of controllable quantum systems, several conceptual challenges emerge in quantum optimal control. Finding optimal control in increasingly large systems while retaining high accuracy requires the number of optimization parameters to scale with the Hilbert-space dimension. This complicates the optimization of parameters and leads to an exponential scaling of computational resources for open-loop optimization. Including experimental constraints makes this problem even more difficult. When restricting pulse amplitudes to take only certain discrete values, which is interesting for cases of limited experimental capabilities and for imposing structures on the pulse sequences, the optimization becomes substantially more challenging [22, 23]. This includes bang–bang or dynamical-decoupling structures [24, 25], which reduce the coupling to the environment and which were shown to correspond to time-optimal control in special cases [26, 27]. These challenges call for novel control-

optimization schemes for enabling both current and future generations of quantum devices.

In this article, we introduce a family of efficient parametrized pulse sequences that address the above challenges and solves the long-standing problem of finding an optimal pulse structure for quantum optimal control [7, 28]. The pulse sequences are assembled in N_L layers, each of which is a sequence of N_P random constant-amplitude pulses (the layer size) characterized by one optimization parameter. We focus on two particular powerful random-layer (RALLY) methods: RALLY_T and RALLY_A. RALLY_T optimizes the time durations of the layers keeping the random amplitudes fixed, while RALLY_A optimizes a joint factor that scales the randomly chosen amplitudes in a layer keeping the pulse durations fixed (see Fig. 1). We first rigorously show that, upon sampling over the RALLY optimization parameters *and* control amplitudes, the ensemble of unitaries reachable by this pulse-sequence structure converges exponentially fast with $N_P N_L$ to the Haar-random ensemble [29]. This provides exponential expressivity, i.e., efficient exploration of the entire unitary space. However, when considering all those random variables as optimization parameters to solve a generic task, this leads to a challenging optimization problem in practice. This motivates our layered pulse-sequence structure, where groups of N_P pulses share a joint parameter. We provide compelling numerical evidence that, for the overwhelming majority of *individual random choices of control amplitudes*, the ensemble of reachable unitaries exhibits the same convergence behavior with $N_P N_L$ even though we sample only N_L RALLY parameters. This feature of grouping pulses is key to ensure that the expressivity of our

* walter.hahn@iaf.fraunhofer.de

pulse sequences increases with the layer size N_P without changing the number of optimization parameters N_L , and enables efficient optimization. For RALLY_T, this even holds when the pulse amplitudes are randomly chosen from a discrete set of values. RALLY_A, in turn, can be neatly incorporated into the existing CRAB [6] and dCRAB [7] algorithms by interpreting it as a new enhanced set of basis functions.

Beyond exponential expressivity, the RALLY_T method provides other important advantages: Constraints of the experimental setting, such as a finite bandwidth, are readily accommodated. Further, an additional penalty term on the total time duration can be introduced to reduce the total pulse-sequence duration without compromising optimization efficiency. RALLY_T is computationally efficient to simulate making it applicable to larger systems than common quantum optimal control algorithms. Both methods RALLY_T and RALLY_A can be used in gradient-based and gradient-free optimization, hence they can be applied in closed-loop and open-loop pulse optimization.

To demonstrate the performance of the RALLY methods, we perform numerical simulations on three tasks: unitary synthesis of a three-qubit gate and ground-state preparation on a globally driven Rydberg-atom platform, and state transfer in an Ising spin chain. For these problems, the RALLY methods approach an information-theoretic lower bound on the number of optimization parameters [30, 31] and exhibit clear advantages when compared to other commonly used algorithms. In particular, we observe that, in gradient-free optimization, both RALLY methods achieve several orders of magnitude higher accuracies with fewer figure-of-merit evaluations. We demonstrate that, with minor modifications, RALLY_T yields pulse sequences with reduced total time. By employing a gradient-based optimization routine and randomly selecting pulse amplitudes from two values, RALLY_T accurately optimizes systems with two more qubits within the same time budget than the GRAPE algorithm [5] while also accommodating realistic bandwidth limitations. RALLY_A usually yields slightly more accurate results than RALLY_T.

The next section (Sec. II) provides introductory remarks on quantum optimal control. In Sec. III, we introduce the RALLY methods and discuss their advantages. Section IV presents benchmarks of the RALLY methods. We conclude in Sec. V.

II. INTRODUCTORY REMARKS

We consider a quantum system described by a Hamiltonian operator of the form $\mathcal{H}(t) = \mathcal{H}_0 + u(t)\mathcal{H}_c$, where \mathcal{H}_0 is usually referred as the drift Hamiltonian and \mathcal{H}_c is the control Hamiltonian with the corresponding time-dependent control field $u(t)$ [32]. The drift Hamiltonian governs the evolution of the system in the absence of the control field. We define a pulse as the evolution over

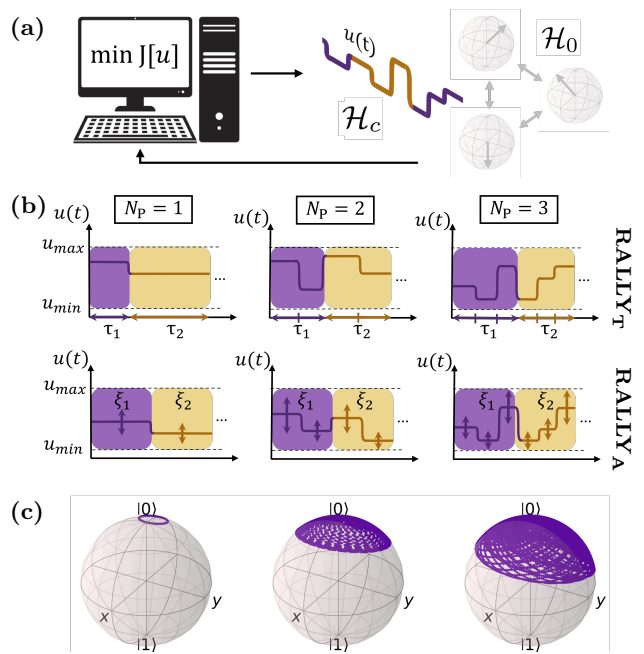


FIG. 1. (a) Sketch of a pulse-optimization procedure in quantum optimal control. The dynamics of a quantum system with internal Hamiltonian \mathcal{H}_0 is controlled by applying a pulse sequence $u(t)$ that couples to the system via the control Hamiltonian \mathcal{H}_c . The optimal pulse is found by minimizing a figure of merit $J[u]$ in a feedback loop. (b) In RALLY, the control pulse sequence $u(t)$ is grouped into N_L layers (different colors) with N_P pulses per layer. The pulse amplitudes are chosen randomly. In RALLY_T, the layer durations τ_ℓ are optimized. In RALLY_A, the scaling factors ξ_ℓ of the control amplitudes are optimized. (c) Illustration of how the expressivity increases for larger N_P . When changing τ , the dynamics of a single layer traces out a trajectory on the Bloch sphere. With increasing N_P , this trajectory becomes more complex and covers an increasing area of the Bloch sphere. Single-spin trajectories are shown for the Hamiltonian $\mathcal{H}(t) = 5\sigma_z + u(t)\sigma_x$, starting from the initial state $|0\rangle$, with evolution time $\tau = 100$ and $u(t)$ composed of fixed control amplitudes whose values are randomly sampled from the interval $[-2, 2]$.

a period of time when the control field $u(t)$ and, hence, also the Hamiltonian $\mathcal{H}(t)$ is constant. Quantum optimal control methods aim to steer the system by means of the control field $u(t)$ to optimize a functional $J[u]$ (figure of merit), which describes the problem to be solved.

A. Necessary conditions for solving quantum optimal control problems

Finding accurate solutions to a quantum control problem requires meeting the following complementary requirements.

a. Reachability: Reachability concerns the question whether a specific target state or unitary is reachable

in principle for the given the control possibilities. A stronger requirement going beyond reachability is full controllability which corresponds to the ability to generate any unitary transformation. The common test for controllability is to investigate whether the dynamical Lie algebra spans the traceless skew-Hermitian algebra $\mathfrak{su}(N)$ [33], see Appendix A for more details. The direct condition for reachability is generally more difficult to certify than establishing full controllability [34].

b. Quantum speed limits: The minimal evolution time required to approximate either a target state or a target unitary transformation is generally bounded from below by constraints from the Hamiltonian and the initial conditions [35–38]. Such lower bounds are formalized by different quantum speed limits depending on the task, the energy spectrum, and specified initial and target conditions [39–43]. For example, for arbitrary state-transfer in a spin chain with n spins, access to n control Hamiltonians yields a minimal evolution time that scales linearly with n [44]. To incorporate the geometry induced by the drift and control Hamiltonians, the geodesic length set by the quantum geometric tensor can be considered [45, 46].

c. Information-theoretic constraint: From the information-theoretic perspective, any quantum optimal control approach that aims to reach an arbitrarily high fidelity must entail at least as many independent real optimization parameters as there are real degrees of freedom required for the description of the optimization problem [30, 31]. For example, an arbitrary quantum state in a N -dimensional Hilbert space is described by $2N$ real parameters. Taking into account the normalization condition and the arbitrariness of the global phase, we arrive at $2N - 2$ degrees of freedom, hence at least $2N - 2$ real optimization parameters for an accurate approximation of any target state are required [7, 30, 47]. Similarly, when approximating an arbitrary unitary transformation, the relevant space is $SU(N)$ with $N^2 - 1$ real degrees of freedom. These constraints provide a useful estimate for the required number of optimization parameters. Over-parametrization is considered relative to these constraints.

B. Common quantum optimal control algorithms

Quantum optimal control algorithms can be gradient-free and gradient-based [1, 2]. Gradient-free methods are simple to deploy and flexible for closed-loop optimization because they rely only on figure-of-merit evaluations. However, they typically converge slower than gradient-driven approaches, especially in high-dimensional control spaces. An example is the dCRAB algorithm combined with a Nelder–Mead optimizer [7, 28, 48–50]. Gradient-based techniques converge faster and often scale better for larger systems but obtaining reliable gradients and maintaining differentiability make their direct use in closed-loop calibration difficult. The GRAPE algorithm is a canonical example [5, 8, 51]. We detail dCRAB

and GRAPE algorithms in Appendix B and use them for benchmarking the RALLY methods.

III. RANDOM-LAYER METHODS

A. Definition of the RALLY pulse sequences

The pulses in a RALLY pulse sequence are arranged in layers

$$U_{\text{R}}(\theta_1, \dots, \theta_{N_{\text{L}}}) = \prod_{\ell=1}^{N_{\text{L}}} U_{\ell}(\theta_{\ell}), \quad (1)$$

where $U_{\ell}(\theta_{\ell})$ is the propagator describing layer ℓ with optimization parameter θ_{ℓ} and N_{L} is the total number of layers. For each layer, $U_{\ell}(\theta_{\ell})$ is a concatenation of N_{P} constant-amplitude pulses (layer size), where the pulse amplitudes are chosen randomly from a predefined set.

We propose two RALLY methods with optimization parameters being either layer durations ($\theta_{\ell} = \tau_{\ell}$) in RALLY_T or scaling factors ($\theta_{\ell} = \xi_{\ell}$) for control amplitudes in RALLY_A, cf. Fig. 1. We denote the corresponding propagators as $U_{\text{R},\text{T}}(\tau_1, \dots, \tau_{N_{\text{L}}})$ and $U_{\text{R},\text{A}}(\xi_1, \dots, \xi_{N_{\text{L}}})$, respectively. For $U_{\text{R},\text{T}}(\tau_1, \dots, \tau_{N_{\text{L}}})$, we define

$$U_{\text{R},\text{T}}(\boldsymbol{\tau}) = \prod_{\ell=1}^{N_{\text{L}}} \prod_{p=1}^{N_{\text{P}}} \exp \left[-i \frac{\tau_{\ell}}{N_{\text{P}}} (\mathcal{H}_0 + u^{(\ell,p)} \mathcal{H}_c) \right], \quad (2)$$

where $\boldsymbol{\tau} = (\tau_1, \dots, \tau_{N_{\text{L}}})$ and pulse durations of all pulses in a layer are chosen to be the same τ_{ℓ}/N_{P} for simplicity [52]. For $U_{\text{R},\text{A}}(\xi_1, \dots, \xi_{N_{\text{L}}})$, we define

$$U_{\text{R},\text{A}}(\boldsymbol{\xi}) = \prod_{\ell=1}^{N_{\text{L}}} \prod_{p=1}^{N_{\text{P}}} \exp \left[-i \Delta t (\mathcal{H}_0 + \xi_{\ell} u^{(\ell,p)} \mathcal{H}_c) \right], \quad (3)$$

where $\boldsymbol{\xi} = (\xi_1, \dots, \xi_{N_{\text{L}}})$ and all pulses have the same time duration Δt for simplicity. Importantly, for both pulse sequences, the amplitudes of the individual pulses $u^{(\ell,p)}$ are randomly chosen. Note that, due to the presence of the drift Hamiltonian \mathcal{H}_0 , the two propagators $U_{\text{R},\text{T}}(\boldsymbol{\tau})$ and $U_{\text{R},\text{A}}(\boldsymbol{\xi})$ are generally different. Both propagators depend on the control-field amplitudes $u^{(\ell,p)}$ but we indicate this dependence only when necessary.

The RALLY_A propagator $U_{\text{R},\text{A}}(\boldsymbol{\xi})$ can be viewed as a new basis choice for the CRAB [6] or dCRAB [7] algorithms with control field $u(t) = \sum_{\ell} \xi_{\ell} \phi_{\ell}(t)$, where each basis function $\phi_{\ell}(t)$ is a concatenation of piecewise-constant segments with amplitudes $\{u^{(\ell,p)}\}_p$.

B. Convergence properties of RALLY pulse sequences

To investigate the convergence properties of the RALLY pulse sequences, let us consider the set of unitary

operators $U_R(\boldsymbol{\theta})$ reachable by varying the optimization parameters $\boldsymbol{\theta}$ (with $\boldsymbol{\theta} = \boldsymbol{\tau}$ for $U_{R,T}(\boldsymbol{\tau})$ and $\boldsymbol{\theta} = \boldsymbol{\xi}$ for $U_{R,A}(\boldsymbol{\xi})$). The main question is whether the ensemble of unitaries generated by $U_R(\boldsymbol{\theta})$ approximates a Haar-random ensemble on $U(N)$, which is the uniform distribution over the unitary group. Exhibiting properties of the Haar ensemble entails a uniform coverage of the unitary group, thereby making the approximation of an arbitrary target unitary more accurate.

In the following, we first discuss and analytically prove a theorem showing that the ensemble of reachable unitaries approaches the Haar ensemble exponentially with $N_L N_P$ when, in addition to the optimization parameters $\boldsymbol{\theta}$ of the RALLY pulse sequences, the pulse amplitudes $u^{(\ell,p)}$ are also considered optimization parameters. Then, we provide compelling numerical evidence that the conclusions of the theorem hold even for almost any random choice of $u^{(\ell,p)}$, thereby arriving at the setting of the RALLY methods. This corresponds to typicality of randomly chosen unitaries similar to the typicality properties of randomly chosen quantum states, e.g., canonical typicality [53–55].

Let us start by considering the following important theorem: Consider a quantum system being fully controllable. Then, the ensemble of unitaries reachable by the RALLY propagator $U_R(\boldsymbol{\theta})$, where *both* optimization parameters $\boldsymbol{\theta}$ and control amplitudes $u^{(\ell,p)}$ are sampled from a continuous distribution, converges exponentially fast in the number of pulses $N_L N_P$ to the uniform Haar ensemble. Moreover, if control amplitudes are drawn from a set of discrete values, the theorem holds by considering a weaker convergence criterion. For a rigorous treatment and a proof, we refer the reader to Appendix C.

We corroborate the above theorem with numerical simulations of an Ising chain consisting of $n = 3$ spins-1/2 in a longitudinal and transverse magnetic field

$$\mathcal{H}_1 = \sum_{i=1}^n h_{ix} \sigma_{ix} + \sum_{i=1}^n h_{iz} \sigma_{iz} + J(t) \sum_{i=1}^{n-1} \sigma_{ix} \sigma_{(i+1)x}, \quad (4)$$

where h_{ix} (h_{iz}) are the spin-dependent magnetic-field components along the x -axis (z -axis), $\sigma_{i\alpha}$ is the Pauli operator of spin i along direction α and the interaction coefficient $J(t)$ is the time-dependent control field. The components h_{ix} and h_{iz} are randomly chosen from the interval $[0.5, 1]$, which ensures that no symmetries exist and that the system is fully controllable [7]. We present the analysis for RALLY_T but, based on the optimization performance described below, we anticipate similar convergence behavior for RALLY_A.

We investigate the convergence of the ensemble of reachable unitaries to the Haar ensemble by studying the convergence of the first four moments of the corresponding distribution, which is equivalent to convergence to unitary designs of up to order 4. The t -th moment converges if and only if the following expression vanishes [56]

$$\delta_t = \left| \mathbb{E}_{x,y \sim \nu} \left[\left| \text{tr}(U_R(x)^\dagger U_R(y)) \right|^{2t} \right] - t! \right|, \quad (5)$$

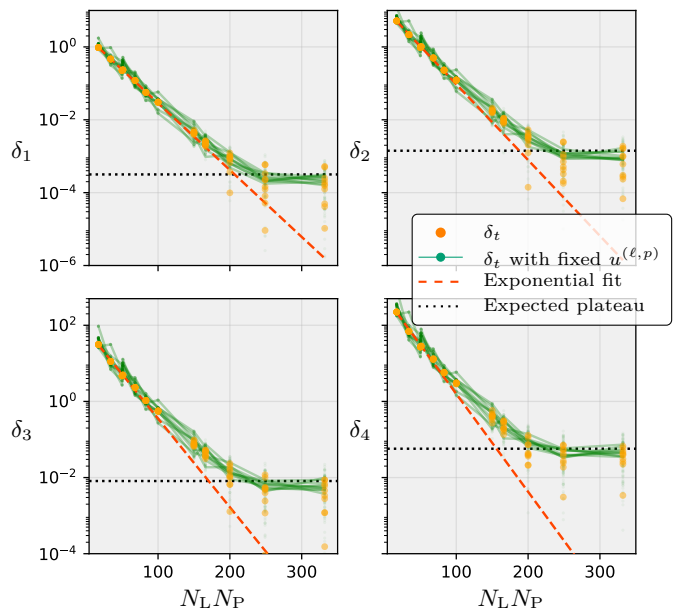


FIG. 2. Exponential convergence of the first four moments of the ensemble of unitaries reachable by the RALLY_T propagator $U_{R,T}$ to the corresponding moments of a Haar random distribution. The difference δ_t (5) between the corresponding moments is shown for $t = 1, 2, 3, 4$ as a function of $N_L N_P$. Orange points show δ_t with layer durations drawn uniformly from $[0, 10]$ and control amplitudes drawn uniformly from $[-1, 1]$. The dashed red line is a linear fit on the logarithmic scale. More importantly, results for δ_t follow the same decay curve also when *only layer durations* are sampled and the control amplitudes are fixed (shown by the 10 green lines). We attribute the fluctuations of the green lines to the finite system sizes, see Appendix E. The plateaus at larger values of $N_L N_P$ are due to the finite sample size and they are consistent with the expected values from the Haar distribution (black dotted lines); see Appendix D for details. For each value of $N_L N_P$, where $N_L \in \{17, 50, 83\}$ and $N_P \in \{1, 2, 3, 4\}$ we use 10^7 samples and average over 10 repetitions for one set of randomly chosen values of h_{ix} and h_{iz} , cf. Eq. (4).

where the expectation is taken over two independent samples, $x, y = (\boldsymbol{\tau}, u^{(\ell,p)}) \sim \nu$, with ν being the joint probability distribution of layer durations and control amplitudes. The numerical results shown in Fig. 2 exhibit an exponential decay of δ_t for the moments $t \leq 4$ with $N_L N_P$, which is in accordance with the theorem.

Remarkably, we observe the same exponential decay also for each *individual random choice* of the control amplitudes as also shown in Fig. 2. At first sight, an exponential decay only with N_L is anticipated because N_L layer durations are optimized. The typical behavior observed for each individual random choice of the control amplitude implies that each individual pulse entering a RALLY pulse sequence contributes equally to the expressivity of the corresponding propagator, hence the exponential decay with $N_L N_P$. We attribute the small deviations of δ_t for the individual random choices of the control amplitudes from the exponential decay to the finite size

of the quantum system. When considering the Ising spin chain for two spins instead of three, the deviations from the exponential decay become larger, cf. Appendix E. This typical behavior provides the foundation for the efficacy of the RALLY methods and it is somewhat similar to the typicality of randomly chosen quantum states, e.g., canonical typicality [53–55].

From the above results follows that the convergence properties of the RALLY pulse sequences can be enhanced by increasing the layer size N_P without changing the number of optimization parameters N_L . Thereby, over-parametrization can be avoided at the expense of a larger total number of pulses. Qualitatively, this can be understood on the basis of a single-spin dynamics, cf. Fig. 1c. For $N_P = 1$, the spin dynamics within a layer is confined to a circle on the Bloch sphere for any random choice of the pulse amplitude. For $N_P > 1$, the dynamics is more complicated because the effective Hamiltonian \mathcal{H}_{eff} for a layer is time-dependent due to the concatenation of N_P rotations around different axes. For example, this corresponds to $U_{R,T}(\boldsymbol{\tau}) = \prod_{\ell=1}^{N_L} \exp[-i\tau_\ell \mathcal{H}_{\text{eff}}(\tau_\ell)]$ for RALLY_T, cf. Eq. (2). Therefore, the corresponding path covers a larger region of the Bloch sphere in a loose analogy to space-filling curves that explore a two-dimensional manifold, leading to a more efficient exploration of the unitary group by U_R . This intuition naturally extends to higher-dimensional settings.

C. Advantages of the RALLY_T method

The key feature of the RALLY_T method is that the pulse amplitudes $u^{(\ell,p)}$ are randomly chosen *prior* to the actual optimization and remain unchanged thereafter. Therefore, by tailoring the predefined set from which the coefficients $u^{(\ell,p)}$ are drawn, one can explicitly enforce hardware constraints, such as a maximum-amplitude condition $|u^{(\ell,p)}| \leq u_{\text{max}}$, or restrict the pulse amplitudes to a discrete set of allowed values. The latter is interesting, for example, for cases of limited experimental capabilities and for imposing particular structures on the pulse sequences. For example, dynamical-decoupling structures [24] are known to reduce the coupling to the environment. Further, pulse sequences similar to bang-bang $u^{(\ell,p)} \in \{\pm u_{\text{max}}\}$ [25] and bang-singular-bang protocols $u^{(\ell,p)} \in \{0, u_{\text{max}}\}$ [26] were shown to be time optimal for the rotation of a single spin-1/2 [27].

Sampling control amplitudes $u^{(\ell,p)}$ randomly and optimizing layer durations enable resource-efficient simulations for RALLY_T. Specifically, for the RALLY_T propagator $U_{R,T}$ (2), the Hamiltonians $\mathcal{H}^{(\ell,p)} = \mathcal{H}_0 + u^{(\ell,p)}\mathcal{H}_c$ can be diagonalized in advance, allowing the figure of merit and its gradient to be evaluated across parameter values using only matrix–matrix or matrix–vector multiplications. This is particularly advantageous when $u^{(\ell,p)}$ are drawn from a small discrete set. This contrasts with methods that require repeated matrix exponentials or diagonalizations for each figure-of-merit evaluation.

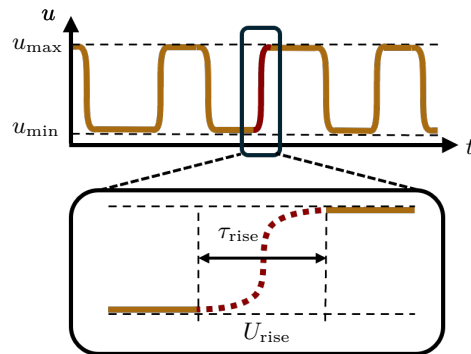


FIG. 3. Illustration of the interpolation between successive control amplitudes to accommodate the hardware’s finite bandwidth in RALLY_T. A limited bandwidth $\Delta\Omega$ imposes a finite rise time τ_{rise} , implemented in the pulse via an interpolating function that depends only on the amplitudes and not on the pulse durations. Because RALLY_T samples amplitudes before optimization and optimizes time durations, the propagators for these interpolations, denoted U_{rise} , can be precomputed and included in the figure of merit, and eventually in its gradient, as constants.

Finite-bandwidth constraints, which typically pose challenges for piecewise-constant pulse sequences, are readily accommodated in RALLY_T. An interpolation between the pulse amplitudes that reflects hardware limitations can be introduced as sketched in Fig. 3. Unitary propagators of the interpolating steps can be included in the overall RALLY_T propagator $U_{R,T}$ (2) with negligible computational overhead. Since the pulse amplitudes are chosen prior to the optimization and the unitary transformations describing the interpolations do not depend on the pulse durations, they can be numerically calculated in advance and reused during the optimization.

An additional penalty term (for example, of the form $\sum_{\ell=1}^{N_L} \tau_\ell$) allows for reducing the total pulse-sequence duration along with the actual optimization. For quantum devices, which restrict changes of the control amplitudes to periodic grid points in time [57], the optimized layer durations can be rounded to the nearest point in time while assuming that the solution found is sufficiently stable with respect to small perturbations in time, cf. Appendix F. A subsequent fine-tuning optimization with RALLY_A for the control amplitudes could also be performed.

IV. NUMERICAL SIMULATIONS AND BENCHMARKING

We demonstrate the advantages of the RALLY methods by means of numerical simulations for three control tasks: unitary synthesis, ground-state preparation, and state transfer. For unitary synthesis and ground-state preparation, we consider a globally driven Rydberg-atom platform, and for state transfer, an Ising spin chain.

To benchmark RALLY methods, we compare its performance to that of the dCRAB and GRAPE algorithms.

A. Unitary synthesis of a three-qubit gate

We now focus on the unitary synthesis on a globally-driven Rydberg-atom simulator platform with n atoms (qubits), for which the Hamiltonian reads [58]

$$\begin{aligned} \mathcal{H}_R(\Omega, \Delta) &= \mathcal{H}_0 + \Omega \mathcal{H}_x - \Delta \mathcal{H}_z \\ &= \sum_{i < j}^n J_{ij} n_i n_j + \Omega \sum_{i=1}^n \sigma_{ix} - \Delta \sum_{i=1}^n \sigma_{iz}, \end{aligned} \quad (6)$$

where $J_{ij} \cong 1/r_{ij}^6$ describes the Van der Waals interaction between atoms i and j with r_{ij} being the interatomic distance, $n_i = (\mathbf{1} - \sigma_{iz})/2$ the occupation operator; and Ω and Δ are the Rabi frequency and the detuning of the external global driving, respectively. The Rydberg-atom positions remain unchanged during the dynamics. They are chosen such that the Hamiltonian in Eq. (6) does not exhibit any symmetries (see Appendix H) and the system is fully controllable, as we verified by means of dynamical-Lie-algebra analysis. We set the global Rabi frequency to $\Omega = 1$ MHz for the entire pulse sequence; hence, the detuning Δ is the only control field [$\mathcal{H}_R(\Omega, \Delta) = \mathcal{H}_R(\Delta)$] varied within the hardware limits (see Appendix G).

For the unitary-synthesis problem, we consider the figure of merit [59]

$$J_u[u] \equiv 1 - \frac{1}{2^{2n}} \left| \text{Tr}(U_T^\dagger U[u]) \right|^2, \quad (7)$$

which is sometimes referred to as unitary infidelity. The target unitary is the three-qubit gate

$$U_T = \text{CNOT}_{1,2} \otimes \mathbf{1}_3. \quad (8)$$

Since the driving in the Rydberg system equally affects all three participating qubits (atoms) and the interactions between the qubits are always present, the challenge is not only to implement the $\text{CNOT}_{1,2}$ gate but also to leave the third qubit unchanged at the same time. Problems of such kind are important, for example, to realize precise gates on a quantum computer while suppressing crosstalk, i.e., without affecting nearby qubits (see, for example, Ref. [60]).

1. Performance of the RALLY methods

The results shown in Fig. 4 for the unitary infidelity for different N_L and $N_P = 5$ indicate that the RALLY methods become highly accurate once the number of optimization parameters surpasses the information-theoretic lower bound $N^2 - 1 = 63$. When compared to the dCRAB algorithm, both with Fourier and piecewise-constant (pwc) basis, the RALLY methods are more accurate while requiring fewer figure-of-merit evaluations.

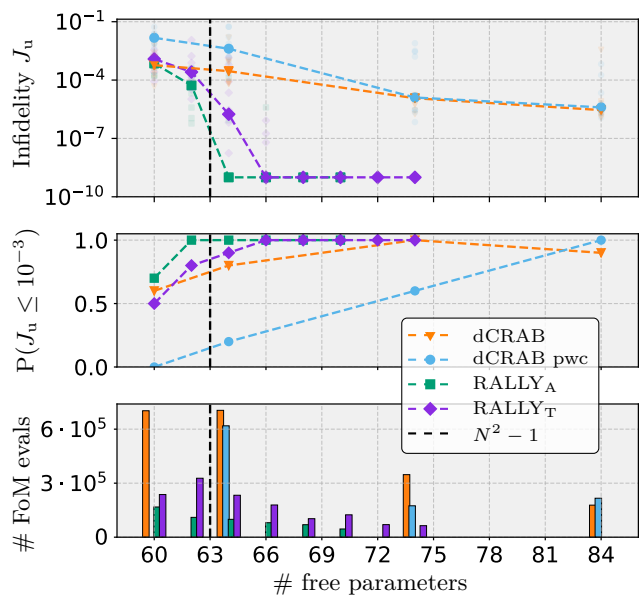


FIG. 4. Performance of RALLY methods for the unitary synthesis of a 3-qubit gate, cf. Eqs. (8), in a globally-driven Rydberg-atom platform. As a function of the number of optimization parameters (N_L for RALLY), the figure shows the median unitary infidelity J_u (7) (top), success probability of achieving $J_u \leq 10^{-3}$ over 10 independent runs (middle) and the median number of figure-of-merit evaluations required to reach $J_u \leq 10^{-3}$ (bottom). The RALLY methods with $N_P = 5$ rapidly converge to the target precision of 10^{-9} and efficiently saturate the information-theoretic lower bound (vertical dashed line) on the number of optimization parameters, whereas dCRAB with Fourier and piecewise constant (pwc) bases converges more slowly. The RALLY methods also need fewer figure-of-merit (FoM) evaluations than dCRAB. Missing bars in the bottom part correspond to cases where no successful optimizations were achieved. All methods use the same optimizer (adaptive Nelder–Mead) and identical stopping criteria.

The RALLY methods also exhibit higher success rates for the infidelity to be below 10^{-3} . This indicates that, for practical applications where an infidelity of about 10^{-3} is sufficient, RALLY is advantageous in terms of the success rate and the number of figure-of-merit evaluations required.

For the above results, the Nelder–Mead optimization algorithm was used with identical settings for both RALLY and dCRAB (see Appendix H for further details). The values for the detuning Δ were limited to the interval $\Delta \in [-10, 10]$ MHz, which corresponds to realistic hardware constraints [61]. To ensure that these constraints are not violated in RALLY_A, we enforce $\xi \in [0, 1]^{N_L}$. The total evolution time T for dCRAB and RALLY_A was chosen to be approximately the same as for RALLY_T. For the Fourier basis, the maximum bandwidth $\Delta\Omega$ is chosen to satisfy $\Delta\Omega T \geq N^2 - 1$ [7, 31], ensuring that the time–bandwidth product does not limit the information content of the control pulse.

2. Enhancing expressivity of RALLY with larger N_P

We now demonstrate that enhancing the expressivity of $U_{R,T}(\boldsymbol{\tau})$ by increasing the layer size N_P improves the probability of successful convergence for the optimization problem. Similar results can be shown for RALLY_A. Figure 5 shows the success probability for achieving $J_u[u_k] \leq 10^{-3}$ as a function of the total pulse-sequence duration and the layer size N_P . The total number of optimization parameters is $N_L = 66$, which is slightly larger than its theoretical lower bound of 63.

The results in Fig. 5 imply that a layer size $N_P = 3$ is sufficient to achieve accurate approximation at a relatively small total pulse-sequence duration, which corresponds to three pulses per optimization parameter (layer) [62]. These results also confirm that the enhanced performance of the RALLY methods at $N_P > 1$ is not due to longer time durations of pulse sequences, which could be caused by the higher number of pulses. We attribute the low performance of RALLY at relatively small N_P to an insufficient expressivity of the propagator $U_{R,T}(\boldsymbol{\tau})$. Further, the low performance of RALLY_T at small total pulse-sequence durations ($\lesssim 60\mu\text{s}$) is presumably caused by quantum speed limits.

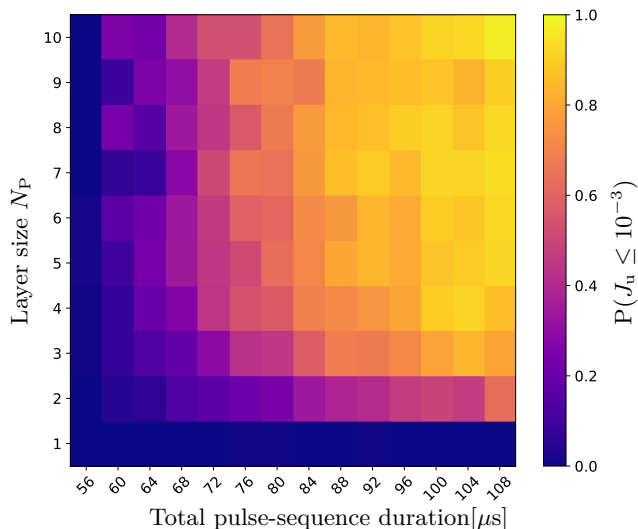


FIG. 5. Success probability of achieving $J_u \leq 10^{-3}$ for different total pulse-sequence durations and layer sizes N_P using RALLY_T. The results indicate that the effectiveness of the method improves as the layer size increases while keeping the total pulse-sequence duration fixed. For each pair of total duration and N_P , we run at least 100 optimizations with different random initializations of τ_ℓ and group the results by their final total pulse-sequence durations. Due to the abundance of local minima in the optimization landscape, the layer durations typically remain close to their initial values, so the heatmap effectively samples different total durations at fixed N_P .

3. Reducing the total pulse-sequences time duration with an additional penalty term

To reduce the total pulse-sequence time duration $\sum_{\ell=1}^{N_L} \tau_\ell$, RALLY_T offers the possibility to add a quadratic penalty term $(\sum_{\ell=1}^{N_L} \tau_\ell)^2$ to the figure of merit, which is to be minimized. For the unitary-synthesis problem, we hence obtain $J_u[u_k] + \lambda \left(\sum_{\ell=1}^{N_L} \tau_\ell\right)^2$ for the total figure of merit, where λ is the weight of the additional time-reducing term. Thus, a single optimization run with a suitable weight λ can efficiently yield a short pulse sequence and accurate approximation at the same time.

For the unitary-synthesis problem, we obtain a short pulse sequence with a total time duration of about $55\mu\text{s}$ that achieves a unitary infidelity $J_u \leq 10^{-3}$ using $\lambda = 10^{-4}$. This duration exceeds the standard quantum speed limit that ignores the geometry of the drift and control Hamiltonians [43]. Hence, a more appropriate reference value for the globally-driven Rydberg platform may be the geometric speed limit [44, 45].

B. Ground-state preparation for molecules

For the variational ground-state preparation, the figure of merit to be minimized is the energy-expectation value of the target Hamiltonian \mathcal{H}_T

$$J_e[u] \equiv \langle \psi_0 | U^\dagger[u] \mathcal{H}_T U[u] | \psi_0 \rangle, \quad (9)$$

where $|\psi_0\rangle = |0\rangle^{\otimes n}$ is the initial state of the system. Similar problems are considered in variational quantum algorithms such as the variational quantum eigensolver (VQE) [63] and the variational quantum simulation (VQS) [21, 64]. The variational ground-state preparation on the control-pulse level can be reinterpreted as a quantum control problem [65, 66].

Using the RALLY methods, we determine the ground states of the molecules H_2 , NO_3 and CH in numerical simulations of a globally-driven Rydberg-atom platform (6). The minimal meaningful choice of the spin orbitals for the three molecules H_2 , NO_3 and CH results in an increasing Hilbert-space (or symmetry-sector) dimension of 9, 16 and 64, respectively, as detailed in Appendix I. The three molecules also differ in the von-Neumann entanglement S of the corresponding ground states with the average single-qubit (spin-orbital) entanglement: $S \approx 0.1$ for H_2 , $S \approx 0.8$ for NO_3 and $S \approx 0.4$ for CH ; see Appendix J.

The RALLY methods achieve the target precision of 10^{-9} H while approaching the information-theoretic bound for all three molecules as shown in Fig. 6. The RALLY methods also yield more accurate results than dCRAB for the molecules, while requiring fewer figure-of-merit evaluations. Only for the H_2 molecule with the smallest Hilbert-space dimension, dCRAB outperforms the RALLY method in terms of the success rate for achieving $J_e \leq 10^{-3}$. For this comparison, identical opti-

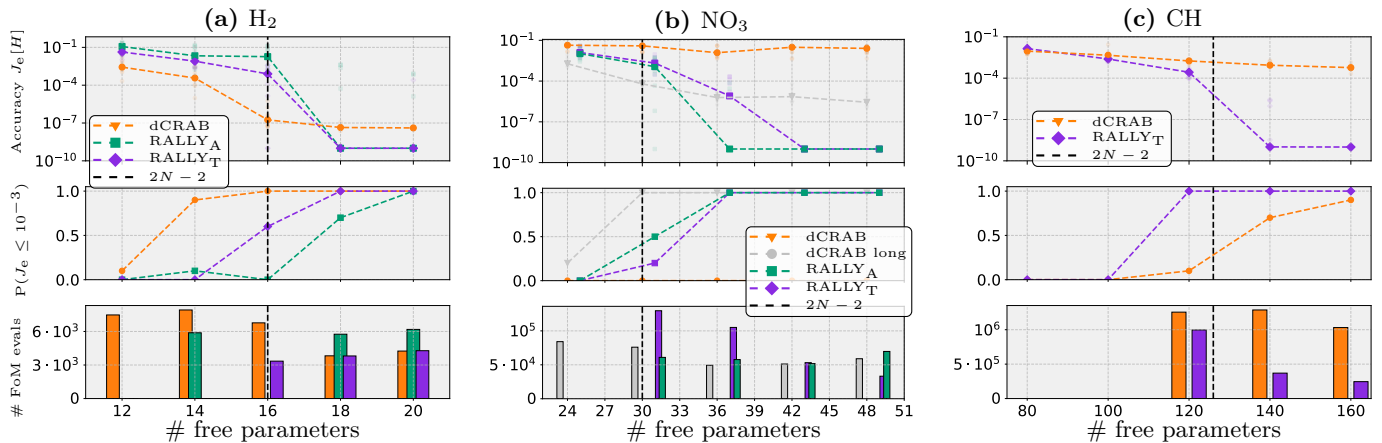


FIG. 6. Performance of RALLY methods and dCRAB for the ground-state preparation for the three molecules H_2 (a), NO_3 (b), and CH (c). RALLY methods achieve the target precision of $J_e \leq 10^{-9}$ H for all three molecules while approaching the information-theoretic bound (dashed vertical line) on the minimum number of parameters with $N_P = 5$. Except for H_2 , RALLY methods converge to target accuracy faster than dCRAB and require fewer figure-of-merit evaluations. Each panel shows, as a function of the number of layers N_L : (top) median ground-state energy accuracy J_e (9), (middle) success probability (over 10 independent runs) of reaching $J_e \leq 10^{-3}$ H, and (bottom) the median number of figure-of-merit J_u evaluations required to reach the same threshold. Missing bars correspond to cases where no successful optimizations were achieved. Both methods use the same optimizer (adaptive Nelder–Mead) and identical stopping criteria. For NO_3 , two dCRAB settings are shown: one with total time $T = 500 \mu\text{s}$ similar to RALLY’s optimized schedule and one with a much longer $T = 3000 \mu\text{s}$ illustrating the need for dCRAB to operate at longer times for this problem. For dCRAB, the Fourier basis was used.

mization algorithms, optimization settings, and convergence criteria were used, as detailed in Appendix I. It is also noteworthy that the simulations using the RALLY_T method terminated two to five times faster than those using the dCRAB and RALLY_A algorithms.

For the NO_3 molecule, the dCRAB algorithm fails to reach an accuracy of 10^{-3} H within a total pulse-sequence duration of $T = 500 \mu\text{s}$, which is comparable to the duration obtained with RALLY_T and equal to that used for RALLY_A, cf Fig. 6b. Accuracy below 10^{-3} H was reached when increasing the total control-field time to $T = 3000 \mu\text{s}$. While the accuracy of the dCRAB algorithm gradually improves when increasing the number of optimization parameters, RALLY methods converge to the target precision once N_L is above the information-theoretic minimum.

C. State transfer in an Ising chain

Let us now consider an Ising chain of n spins-1/2 described by the Hamiltonian (4). We consider a state-transfer problem, when the initial state $|\psi_0\rangle = |0\rangle^{\otimes n}$ must evolve into the n -qubit GHZ state $|\text{GHZ}_n\rangle = \frac{1}{\sqrt{2}}(|0\rangle^{\otimes n} + |1\rangle^{\otimes n})$. The figure of merit is the state-transfer infidelity

$$J_s[u] \equiv 1 - |\langle \text{GHZ}_n | U[u] | \psi_0 \rangle|^2. \quad (10)$$

1. Performance of the RALLY methods

To demonstrate the capabilities of RALLY_T, we (i) restrict the pulse amplitudes to two discrete values $J(t) \in \{+1, -1\}$ and (ii) smoothly interpolate between these two discrete pulse amplitudes, cf. Fig. 3. The latter is to accommodate a finite bandwidth of the experimental setting. As shown in Fig. 7, RALLY_T achieves high-fidelity state transfer on an $n = 6$ Ising chain, where the sigmoid function detailed in Appendix O was used for the interpolation. Once the number of optimization parameters N_L exceeds the information-theoretic minimum, RALLY_T reaches an infidelity of 10^{-7} and lower. Enforcing the above hardware constraints has little effect on the results: RALLY_T exhibits comparable accuracy when randomly choosing the pulse amplitudes from a continuous distribution and excluding the interpolation between pulses. GRAPE and RALLY_A achieve similar infidelities but without accommodating the finite bandwidth and discrete control amplitude values constraints. In fact, the above hardware constraints used for RALLY_T cannot be integrated into GRAPE or RALLY_A without significant computational overhead.

Since analytic expressions for the gradient of the state-transfer infidelity of Eq. (10) can be incorporated in RALLY methods and GRAPE (see Appendices K, M, and L), the above numerical simulations were performed with the gradient-based optimizer L-BFGS-B with the same settings for RALLY methods and GRAPE. As generally expected from gradient-based optimizations, the number of figure-of-merit evaluations is orders of magnitude smaller than for derivative-free optimizations described in the preceding sections.

2. Scaling of the optimization runtime with the system size

Let us now compare the total time required for the pulse-sequence optimizations of the state-transfer problem for both GRAPE and RALLY_T, including any pre- and postprocessing routines. We refer to this total time as the runtime in the following.

Results for the runtime scaling shown in Fig. 8 indicate that, within a maximal runtime of 2×10^4 s, RALLY_T can handle systems with two qubits more than GRAPE. Fitting the results in a double-logarithmic plot by a linear function yields for the runtime scaling the exponents 2.85 ± 0.13 for RALLY_T and 3.53 ± 0.02 for GRAPE. On the basis of theoretical estimates, we expect the scaling to be $\mathcal{O}(N^{3.5})$ for RALLY_T and $\mathcal{O}(N^{4.5})$ for GRAPE, see Appendix N. We attribute this discrepancy to the fact that the theoretical estimates correspond to worst-case estimates and that the scaling of the individual operations has not yet reached its asymptotic regime for the system sizes considered here.

Considering system sizes beyond $n = 10$ qubits is feasible using exact diagonalization of the Hamiltonian but RALLY_T can also be combined with other numerical techniques for the time evolution of quantum systems, such as the Suzuki-Trotter expansion [67] or tensor-network techniques [6, 68].

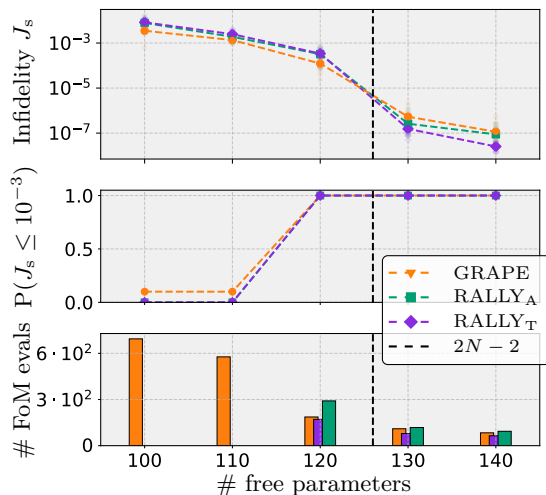


FIG. 7. Result for the state transfer in the Ising chain of $n = 6$ spins-1/2: RALLY methods (with $N_P = 5$) and GRAPE exhibit similar results, whereas RALLY_T better reflects experimental constraints, namely bandwidth-limited pulses (cf. Sec. III) with control amplitudes restricted to two discrete values $\{+1, -1\}$. The individual parts of the figure show as a function of the number of optimization parameters: median state infidelity J_s (10) (top), success probability of achieving $J_s \leq 10^{-3}$ in 10 independent runs (middle), and the median number of figure-of-merit evaluations required to reach $J_s \leq 10^{-3}$ (bottom). Missing bars correspond to cases where no successful optimizations were achieved. All methods use the same gradient-based optimizer (L-BFGS-B) and identical stopping criteria for the optimization.

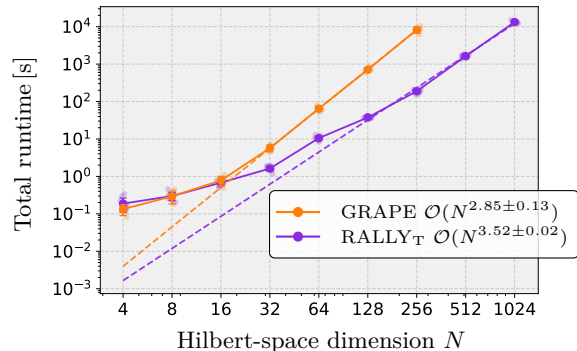


FIG. 8. Runtime scaling to reach a state-transfer infidelity $J_s \leq 10^{-3}$ for different Hilbert-space dimensions $N = 2^n$ for the Ising chain: RALLY_T (violet) and GRAPE (orange). Fitting a linear function to the last four points in the double-logarithmic plot yields for the power-law functions the exponents 2.85 ± 0.13 for RALLY_T and 3.52 ± 0.02 for GRAPE, indicating a better scaling for RALLY_T. Within the maximal runtime of 2×10^4 s, RALLY_T allows to handle systems with two qubits more than GRAPE. Each point is an average over 10 independent calculations, where the same random coefficient sets $h_{ix}, h_{iz} \in [0.5, 1]$ were used for GRAPE and RALLY_T.

V. CONCLUSION

We introduced a family of efficient parametrized pulse sequences based on random layers for quantum optimal control. The efficacy of the random-layers (RALLY) methods is based on two construction principles: (1) *Random unitaries* - The ensemble of reachable unitaries converges exponentially fast to the uniform Haar-random ensemble if the number of pulses per layer N_P is increased, such that the unitary space is explored efficiently. (2) *Layers* - Grouping the pulses into layers allows reducing the number of optimization parameters ensuring efficient optimization. We focused on two RALLY methods: RALLY_T optimizes the time durations of the layers keeping the (potentially discrete) random amplitudes fixed, while RALLY_A optimizes a factor that scales the randomly chosen amplitudes keeping the pulse durations fixed.

We found in numerical simulations that the RALLY methods approach an information-theoretic lower bound on the number of optimization parameters [31]. In the gradient-free setting important for closed-loop optimizations, RALLY methods are orders of magnitude more accurate while also requiring fewer figure-of-merit evaluations when compared to existing algorithms. Further, RALLY_T can be simulated fast due to the possibility of pre-diagonalizing the Hamiltonians of individual pulses. By incorporating an explicit penalty on the total time, RALLY_T provides an efficient route for finding short pulses in large systems, thereby facilitating the study of quantum speed limits. Both RALLY methods are well suitable for both close-loop and open-loop optimizations.

The RALLY methods could be further used for design-

ing efficient quantum-inspired classical optimal-control methods. The application of the random-layer construction concepts to pulse sequences in other bases, for example the Fourier basis, is a further interesting research question. Beyond quantum optimal control, the random-layers design concept can be directly embedded into parameterized circuits for variational quantum algorithms and quantum machine learning. For variational quantum algorithms, the RALLY design concept can be used for enhanced ansätze, for example for the variational quantum eigensolver [66]. For quantum machine learning models like quantum neural networks, RALLY can provide more expressive feature maps or trainable models that avoid over-parameterization.

The source code is published in a GitHub repository [69].

ACKNOWLEDGMENTS

M.D. and W.H. thank R. Zeier and V. V. Dobrovitski for very helpful discussions. M.D. and W.H. acknowledge financial support from the project HPCQS. HPCQS has received funding from the European High-Performance Computing Joint Undertaking (JU) under grant agreement No 101018180. The JU receives support from the European Union's Horizon 2020 research and innovation programme and Germany, France, Italy, Ireland, Austria and Spain in equal parts. The author is solely responsible for its content, it does not represent the opinion of the EuropeanHPC Joint Undertaking and the EuroHPC JU is not responsible for any use that may be made of the information it contains. M.K. acknowledges funding from the European Union's Horizon Europe research and innovation program under grant agreement No 101135699.

Appendix A: Reachability of quantum states

Let us now discuss the problem of the reachability of a target state $|\psi_T\rangle$ when starting from an initial state $|\psi_0\rangle$. System's dynamical Lie algebra (DLA) \mathfrak{g} is defined for the control Hamiltonian \mathcal{H}_c and the drift Hamiltonian \mathcal{H}_0 by [33]

$$\mathfrak{g} \equiv \text{Lie}(\{i\mathcal{H}_0, i\mathcal{H}_c\}) \quad (\text{A1})$$

$$= \text{span} \{i\mathcal{H}_k, [i\mathcal{H}_k, i\mathcal{H}_l], [i\mathcal{H}_k, [i\mathcal{H}_l, i\mathcal{H}_m]], \dots\}, \quad (\text{A2})$$

where $\text{Lie}(\cdot)$ indicates the Lie closure, $k, l, m \in \{0, c\}$, and the span is taken over all possible nested commutators. If the DLA spans the entire skew-Hermitian Lie algebra $\mathfrak{u}(N)$ (or the traceless skew-Hermitian algebra $\mathfrak{su}(N)$) for an N -dimensional Hilbert space, the exponential map generating the corresponding dynamical Lie group yields the full unitary group $\mathbf{U}(N)$ (or the special unitary group $\mathbf{SU}(N)$). This would imply full controllability of the system [33, 70].

In the presence of symmetries that induce invariant subspaces on the Hilbert space, often referred to as

symmetry sectors, the total Hamiltonian can be block-diagonalized. The DLA can in this case be projected onto these sectors to verify their individual controllability. Crucially, if the initial state $|\psi_0\rangle$ and the target state $|\psi_T\rangle$ completely reside within the same symmetry sector and the subspace is controllable, the reachability of the target state from the initial state is guaranteed [34].

Appendix B: dCRAB and GRAPE algorithms

a. dCRAB: The dressed chopped random basis algorithm [7] is based on an expansion of the control field $u(t) = \sum_i c_i \phi_i(t)$ in a truncated basis (e.g. the Fourier basis) [28], where the coefficients c_i are the optimization parameters. One key challenge is the emergence of local traps: spurious local minima induced by truncating the infinite-dimensional space to a finite basis [7]. To avoid false traps, the dCRAB algorithm iteratively introduces new random basis functions $\{\phi_i^{(j)}(t)\}$ in so-called super-iterations and reuses the optimal solution $\tilde{u}^{(j-1)}(t)$ from the optimization in the previous super-iteration

$$u^{(j)}(t) = c_0^{(j)} \tilde{u}^{(j-1)}(t) + \sum_i c_i^{(j)} \phi_i^{(j)}(t), \quad (\text{B1})$$

where only the new coefficients $c_i^{(j)}$ are optimized [48]. The dCRAB algorithm can easily incorporate experimental constraints and it often saturates the information-theoretic lower bounds [6, 19].

b. GRAPE: In the gradient-ascent pulse engineering algorithm [5], the total evolution time T is divided into M equal time windows of duration $\Delta t = T/M$. The control field $u[j]$ is chosen to be piecewise constant for each time window $j = 1, \dots, M$. The Hamiltonian in time window j reads $\mathcal{H}_j \equiv \mathcal{H}_0 + u[j] \mathcal{H}_c$ with the corresponding propagator $U_j \equiv \exp(-i \Delta t \mathcal{H}_j)$ and total time-evolution operator $U(T) = U_M U_{M-1} \dots U_1$. Closed-form expressions for the derivatives can be derived with respect to the optimization parameters $\partial_{u[j]} U(T)$ (for more details, see Appendix L). These analytic gradients enable efficient use of first- and quasi-second-order optimizers (e.g., conjugate gradient, L-BFGS-B [71, 72]) and facilitate the consideration of constraints on the controls.

Appendix C: Proof of convergence of the RALLY propagator U_R

The goal of this section is to prove the theorem stated in Sec. III on the convergence properties of the RALLY propagator U_R . In the following, we distinguish between two cases:

- control amplitudes drawn from a *continuous* probability distribution, and
- control amplitudes drawn from a *discrete* probability distribution (e.g., a finite set of values).

In the continuous case (a), we show below the exponential convergence of the ensemble of unitaries reachable by U_R to the Haar measure with $N_P N_L$. In the discrete case (b), we use a weaker notion of convergence: we limit the proof of convergence to polynomial test functions in the matrix entries (and their complex conjugates) of U_R . In this setting, the results of Ref. [29] still imply exponential convergence in $N_P N_L$ of the expectation values of all such polynomials. This is sufficient for our practical purposes, since figures of merit in quantum optimal control are usually polynomial functions of U_R .

Consider the general form of the RALLY propagator

$$U_R = \prod_{\ell=1}^{N_L} U_\ell, \quad (\text{C1})$$

where each U_ℓ is a layer composed of N_P elementary pulses

$$U_\ell = \prod_{p=1}^{N_P} U_{\ell,p}. \quad (\text{C2})$$

For the proof, we focus on RALLY_T in the following. However, the proof is readily extended to RALLY_A. We divide the proof into three steps: first, we establish key properties of a single layer; second, we lift these properties to the full RALLY propagator; and finally, we analyze convergence to the Haar measure in the continuous case (a) and the discrete case (b).

1. *Single layer propriety:* We treat the layer durations $\{\tau_\ell\}$ and pulse amplitudes $\{u^{(\ell,p)}\}$ as random variables that induce a probability measure ν_ℓ on the unitary group $G = \text{U}(d)$ for the ℓ -th layer via the map

$$(\tau_\ell, \{u^{(\ell,p)}\}_p) \longmapsto U_\ell. \quad (\text{C3})$$

Pulses within a given layer are not independent, because they all share the same random layer duration τ_ℓ . Indeed, each pulse can be written as

$$U_{\ell,p} = \exp \left[-i \frac{1}{N_P} \left(\tau_\ell \mathcal{H}_0 + \tau_\ell u^{(\ell,p)} \mathcal{H}_c \right) \right], \quad (\text{C4})$$

so the relevant random parameters entering the pulses are the products $\tau_\ell u^{(\ell,p)}$. Even if the amplitudes $\{u^{(\ell,p)}\}_p$ are sampled independently, the products $\{\tau_\ell u^{(\ell,p)}\}_p$ are statistically dependent because they all contain the same random factor τ_ℓ . To arrive at a situation in which the individual pulses are statistically independent, we consider conditional probabilities with the condition on the value of the layer duration. For each fixed τ_ℓ , we define the measure $\mu(\tau_\ell)$ on G , which is the distribution of a single pulse $U_{\ell,p}$ when sampling only over the random amplitudes $u^{(\ell,p)}$ with the duration held fixed at τ_ℓ . Conditional on τ_ℓ , the pulses $\{U_{\ell,p}\}_{p=1}^{N_P}$ are i.i.d. with distribution $\mu(\tau_\ell)$.

We then define the conditional measure of the ℓ -th layer, $\nu(\tau_\ell)$, as the distribution of $U_\ell(\tau_\ell)$ at fixed τ_ℓ . Since

a layer is the product of N_P pulses, we have

$$\nu(\tau_\ell) = \mu(\tau_\ell)^{*N_P}, \quad (\text{C5})$$

where $*$ denotes convolution on G (see Ref. [73]).

In analogy to Ref. [29], we work with the Fourier coefficients of these measures. Let \widehat{G} denote the set of inequivalent irreducible unitary representations (irrep) of G , and for $s \in \widehat{G}$ let

$$D^{(s)} : G \rightarrow \text{U}(d_s) \quad (\text{C6})$$

denote a representative of the s -th irrep with dimension d_s . The (matrix-valued) Fourier coefficient of a probability measure f at s is defined by

$$\hat{f}_s := d_s \int_G \overline{D^{(s)}}(U) f(U) dU \in \mathbb{C}^{d_s \times d_s}, \quad (\text{C7})$$

where dU denotes the Haar measure and $\overline{D^{(s)}}$ denotes the element-wise complex conjugation of $D^{(s)}$. The hat indicates the Fourier coefficients in the following. For convolution powers, we have the standard identity (see Eqs. (8)–(9) of Ref. [29])

$$\widehat{\mu^{*m}}_s = d_s \left(\frac{\hat{\mu}_s}{d_s} \right)^m. \quad (\text{C8})$$

Applying this to the conditional layer measure of Eq. (C5) yields

$$\widehat{\nu(\tau_\ell)}_s = \widehat{\mu(\tau_\ell)^{*N_P}}_s = d_s \left(\frac{\widehat{\mu(\tau_\ell)}_s}{d_s} \right)^{N_P}, \quad (\text{C9})$$

where

$$\widehat{\mu(\tau_\ell)}_s := d_s \int_G \overline{D^{(s)}}(U) \mu(\tau_\ell)(U) dU \quad (\text{C10})$$

are the Fourier coefficients of the single-pulse distribution at duration τ_ℓ .

We now consider the unconditional probability measure of a layer obtained by averaging over the random layer duration τ_ℓ . For notational simplicity, we drop the layer index and write $\tau \equiv \tau_\ell$. Let ρ_τ denote the probability distribution of τ , and define the resulting measure of a single layer as

$$\nu := \mathbb{E}_\tau[\nu(\tau)] = \int \nu(\tau) \rho_\tau(\tau) d\tau. \quad (\text{C11})$$

Taking Fourier coefficients and using linearity of the integral, we obtain

$$\hat{\nu}_s = \int \widehat{\nu(\tau)}_s \rho_\tau(\tau) d\tau = \mathbb{E}_\tau \left[d_s \left(\frac{\widehat{\mu(\tau)}_s}{d_s} \right)^{N_P} \right]. \quad (\text{C12})$$

Now, we bound the operator norm of $\hat{\nu}_s$. Using the Jensen inequality and the submultiplicativity $\|AB\| \leq$

$\|A\| \|B\|$, we find

$$\begin{aligned} \frac{\|\hat{\nu}_s\|}{d_s} &\leq \mathbb{E}_\tau \left[\left\| \left(\frac{\widehat{\mu(\tau)_s}}{d_s} \right)^{N_P} \right\| \right] \\ &\leq \mathbb{E}_\tau \left[\left(\frac{\|\widehat{\mu(\tau)_s}\|}{d_s} \right)^{N_P} \right]. \end{aligned} \quad (\text{C13})$$

By the main lemma of Ref. [29] (see the discussion leading to their Eq. (10)), if the support of a probability measure f generates a dense subgroup of G , then for each nontrivial irrep $s \neq 0$ we have

$$\|\hat{f}_s\| < d_s. \quad (\text{C14})$$

We now assume full controllability condition for the RALLY propagator: there exists $0 < \epsilon \leq \tau_{\max} < \infty$ such that, for every $\tau \in [\epsilon, \tau_{\max}]$, the support of $\mu(\tau)$ generates a dense subgroup of $G = \mathbb{U}(d)$. The restriction to strictly positive durations excludes the trivial case in which all pulses with $\tau = 0$ reduce to the identity. The upper bound τ_{\max} is also physically motivated, since pulse durations must be finite in any realistic setting. Under this assumption, Eq. (C14) implies that for every $\tau \in [\epsilon, \tau_{\max}]$ and every nontrivial irrep $s \neq 0$,

$$\|\widehat{\mu(\tau)_s}\| < d_s. \quad (\text{C15})$$

Moreover, the map $\tau \mapsto \|\widehat{\mu(\tau)_s}\|$ is continuous on the compact interval $[\epsilon, \tau_{\max}]$ since it is the composition of continuous maps. Therefore, for each nontrivial s we can define

$$\alpha_s := \max_{\tau \in [\epsilon, \tau_{\max}]} \|\widehat{\mu(\tau)_s}\| < d_s, \quad (\text{C16})$$

which is independent of τ . Inserting this into Eq. (C13) gives, for every nontrivial irrep s ,

$$\frac{\|\hat{\nu}_s\|}{d_s} \leq \left(\frac{\alpha_s}{d_s} \right)^{N_P} < 1. \quad (\text{C17})$$

2. *From single layers to the full RALLY propagator:* Now consider the full RALLY propagator U_R , which is a product of N_L i.i.d. layers, each distributed according to ν . The induced measure on G is the N_L -fold convolution ν^{*N_L} . Applying Eq. (C8) to this convolution gives

$$\widehat{\nu^{*N_L}_s} = d_s \left(\frac{\hat{\nu}_s}{d_s} \right)^{N_L}. \quad (\text{C18})$$

Therefore, for each nontrivial irrep $s \neq 0$ we obtain

$$\begin{aligned} \frac{\|\widehat{\nu^{*N_L}_s}\|}{d_s} &\leq \left\| \frac{\hat{\nu}_s}{d_s} \right\|^{N_L} \\ &\leq \left(\frac{\alpha_s}{d_s} \right)^{N_P N_L}. \end{aligned} \quad (\text{C19})$$

Thus, all nontrivial Fourier coefficients of the distribution of U_R decay exponentially in the total number of pulses $N_P N_L$, with contraction factor $\alpha_s/d_s < 1$.

3. *Convergence to the Haar measure:* At this point, we can use the results of Ref. 29. In case (a), where the control amplitudes are drawn from a continuous distribution, each $\mu(\tau)$ is a continuous probability measure on G with support generating the full group. Reference [29] then implies that the sequence of measures ν^{*N_L} converges uniformly (in the L^∞ norm) to the Haar measure on G , with an exponential rate governed by the bounds in Eq. (C19). \square

In case (b), where the control amplitudes are drawn from a discrete distribution (so that each $\mu(\tau)$ may be a finite sum of delta functions), the same Fourier analysis applies. Uniform convergence of densities is no longer available, but we still obtain exponential convergence for all polynomial test functions, as we now show explicitly. For any polynomial $\Phi : G \rightarrow \mathbb{C}$ define the distance

$$\Delta(\Phi) := \int_G \Phi(U) \nu^{*N_L}(U) dU - \int_G \Phi(U) dU, \quad (\text{C20})$$

so that $\Delta(\Phi) \rightarrow 0$ signifies exact convergence in that weak topology. By Peter-Weyl theorem [73], since Φ is a polynomial, there is a finite set $S \subset \widehat{G}$ and coefficients $c_{jk}^{(s)} \in \mathbb{C}$ with

$$\Phi(U) = \sum_{s \in S} \sum_{j,k=1}^{d_s} c_{jk}^{(s)} D_{jk}^{(s)}(U). \quad (\text{C21})$$

This expansion expresses Φ as a finite linear combination of matrix coefficients of irreducible representations, which play the role of Fourier modes on the group.

We can rewrite the first integral of Eq. (C20) by using the finite Peter-Weyl expansion and the Fourier coefficients of ν^{*N_L} ,

$$\int_G D_{jk}^{(s)}(U) \nu^{*N_L}(U) dU = \frac{1}{d_s} \overline{(\widehat{\nu^{*N_L}_s})_{jk}}. \quad (\text{C22})$$

For the second integral of Eq. (C20), $\int_G D_{jk}^{(s)}(U) dU = 0$ for every nontrivial s because of orthogonality. Moreover, the term with $s = 0$ is equal for both integrals, and then

$$\Delta(\Phi) = \sum_{\substack{s \in S \\ s \neq 0}} \sum_{j,k=1}^{d_s} c_{jk}^{(s)} \frac{1}{d_s} \overline{(\widehat{\nu^{*N_L}_s})_{jk}}. \quad (\text{C23})$$

Taking absolute values and using $|(M)_{jk}| \leq \|M\|$ gives

$$|\Delta(\Phi)| \leq \sum_{\substack{s \in S \\ s \neq 0}} \sum_{j,k=1}^{d_s} |c_{jk}^{(s)}| \frac{\|\widehat{\nu^{*N_L}_s}\|}{d_s}. \quad (\text{C24})$$

Using inequality of Eq. (C19) and defining $\beta_s := \alpha_s/d_s$, we obtain

$$|\Delta(\Phi)| \leq \sum_{\substack{s \in S \\ s \neq 0}} \sum_{j,k=1}^{d_s} |c_{jk}^{(s)}| \beta_s^{N_P N_L}. \quad (\text{C25})$$

Since the index set S is finite, we may introduce the constants

$$C_\Phi := \sum_{\substack{s \in S \\ s \neq 0}} \sum_{j,k=1}^{d_s} |c_{jk}^{(s)}| \quad \text{and} \quad \beta := \max_{\substack{s \in S \\ s \neq 0}} \beta_s < 1. \quad (\text{C26})$$

With this notation, we obtain the compact bound

$$|\Delta(\Phi)| \leq C_\Phi \beta^{N_P N_L}. \quad (\text{C27})$$

Thus, the discrepancy $|\Delta(\Phi)|$ decays exponentially in $N_P N_L$ with respect to the weak topology induced by polynomial test functions. In the language of unitary designs, this implies exponential convergence of the RALLY ensemble to an approximate unitary t -design. \square

In summary, under the assumption of controllability, the distribution of the RALLY propagator U_R converges exponentially fast to the Haar measure on $U(d)$: uniformly in the continuous-amplitude case, and in the sense of all degree- t polynomial test functions (i.e., as an approximate unitary t -design) in the discrete-amplitude case.

Appendix D: Numerical evidence of convergence to Haar ensemble

In this section, we present a numerical criterion to provide evidence of convergence to the Haar measure on $U(d)$. The criterion involves convergence to t -unitary designs via a scalar inequality (Theorem 5.4 of Ref. [56]), originally proved for finite weighted sets and here extended to general probability measure. It is convenient for numerical calculations because it depends only on pairwise overlaps of unitaries and can be estimated directly from samples.

Let us define the positive constant

$$\gamma(t, d) := \int_{U(d)} dU |\text{tr}[U]|^{2t}. \quad (\text{D1})$$

If $t \leq d$, this integral is equal to $t!$ [56].

Theorem D.1 (Finite uniform-weight t -design bound). Let $X \subset U(d)$ be a finite set with sample size $N := |X|$, and consider X with the uniform weights

$$w(x) = \frac{1}{N} \quad (x \in X). \quad (\text{D2})$$

Then for any integer $t \geq 1$,

$$\frac{1}{N^2} \sum_{x,y \in X} \left| \text{tr} [U(x)^\dagger U(y)] \right|^{2t} \geq \gamma(t, d), \quad (\text{D3})$$

with equality if and only if X is a t -design.

Proof: (See Ref [56]). \square

Theorem D.2 (Continuous measure version). Let ν be any probability measure on $U(d)$, and let $t \geq 1$. Define

$$F_t(\nu) := \iint_{U(d) \times U(d)} \left| \text{tr} [U(x)^\dagger U(y)] \right|^{2t} d\nu(x) d\nu(y). \quad (\text{D4})$$

Then

$$F_t(\nu) \geq \gamma(t, d), \quad (\text{D5})$$

with equality if and only if ν is a unitary t -design.

Proof: (Same of Ref [56], replace sums by integrals). \square

The double integral $F_t(\nu)$ can be approximated numerically by Monte-Carlo sampling: draw M independent pairs (U_i, V_i) from the product measure $\nu \otimes \nu$ and form the unbiased estimator

$$\hat{F}_{t,M} := \frac{1}{M} \sum_{i=1}^M X_i \quad \text{with} \quad X_i := \left| \text{tr}(U_i^\dagger V_i) \right|^{2t}. \quad (\text{D6})$$

The strong law of large numbers implies $\hat{F}_{t,M} \rightarrow F_t(\nu)$ as $M \rightarrow \infty$, and the central limit theorem yields the approximate sampling distribution

$$\hat{F}_{t,M} \approx \mathcal{N}\left(F_t(\nu), \frac{\sigma_t^2}{M}\right), \quad \sigma_t^2 := \text{Var}\left(\left| \text{tr}(U^\dagger V) \right|^{2t}\right), \quad (\text{D7})$$

for large M . Finite sampling may produce a violation of the inequality $\hat{F}_{t,M} < \gamma(t, d)$ due to sampling noise. A robust numerical quantity is, therefore, the absolute deviation

$$\delta_t := \left| \hat{F}_{t,M} - \gamma(t, d) \right|. \quad (\text{D8})$$

The typical magnitude of the sampling fluctuations of δ_t are of the order σ_t/\sqrt{M} . Thus, when plotting δ_t , one expects a plateau of the order of this statistical uncertainty. If U and V are independently sampled from the Haar measure on $U(d)$ with $d \geq 4$, as in the main text, one finds (see Ref. [74])

$$\text{Var}\left(\left| \text{tr}(U^\dagger V) \right|^2\right) = 1, \quad (\text{D9})$$

$$\text{Var}\left(\left| \text{tr}(U^\dagger V) \right|^4\right) = 20, \quad (\text{D10})$$

$$\text{Var}\left(\left| \text{tr}(U^\dagger V) \right|^6\right) = 658, \quad (\text{D11})$$

$$\text{Var}\left(\left| \text{tr}(U^\dagger V) \right|^8\right) = 32748. \quad (\text{D12})$$

Appendix E: Convergence to Haar ensemble for individual random choices of pulse amplitudes

As shown in Fig. 2, δ_t follows the same exponential decay for each individual random choice of the pulse amplitudes as δ_t averaged over random choices of the pulse

amplitudes. The small deviations from the exponential decay for the individual random choice of the pulse amplitudes were attributed to the finite size of the spin system. Indeed, when considering only two qubits instead of three for the Ising spin chain, the deviations significantly increase as shown in Fig. 9.

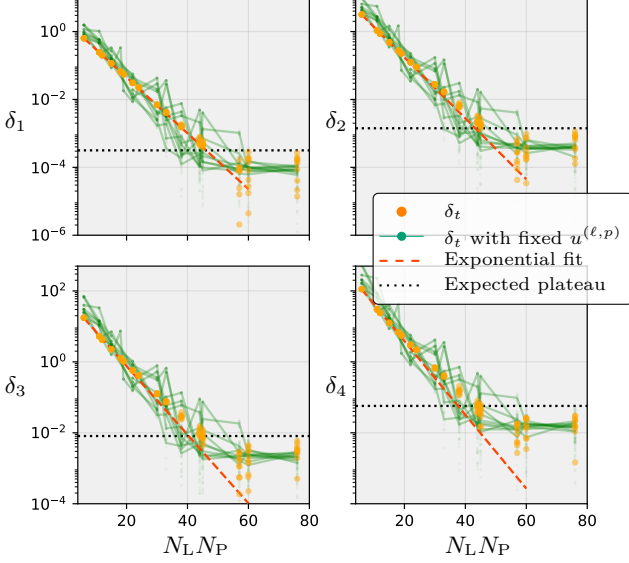


FIG. 9. Same as Fig. 2 but for a two-qubit system: Exponential convergence of the first four moments of the ensemble of unitaries reachable by the RALLY_T propagator $U_{R,T}$ to the corresponding moments of a Haar random distribution. The difference δ_t (5) between the corresponding moments is shown for $t = 1, 2, 3, 4$ as a function of $N_L N_P$. Orange points show δ_t with layer durations drawn uniformly from $[0, 10]$ and control amplitudes drawn uniformly from $[-1, 1]$. The dashed red line is a linear fit on the logarithmic scale. More importantly, results for δ_t follow the same decay curve also when *only layer durations* are sampled and the control amplitudes are fixed (shown by the 10 green lines). We attribute the fluctuations of the green lines to the finite system sizes. The plateaus at larger values of $N_L N_P$ are due to the finite sample size and they are consistent with the expected values from the Haar distribution (black dotted lines); see Appendix D for details. For each value of $N_L N_P$, where $N_L \in \{6, 11, 15, 19\}$ and $N_P \in \{1, 2, 3, 4\}$, we use 10^8 samples and average over 10 repetitions for one set of randomly chosen values of h_{ix} and h_{iz} , cf. Eq. (4).

Appendix F: Robustness of RALLY_T solutions

In this section, we analyze how perturbations in pulse durations and control amplitudes affect the optimized solutions of RALLY_T. We first derive a perturbative bound on the deviation of the total propagator and then relate this deviation to the change in state-transfer infidelity (10). Finally, we compare these predictions with results of numerical simulations of the Ising spin chain (4).

Let us consider the RALLY_T propagator (2)

$$U_{R,T} = \prod_{p=1}^{N_L} \prod_{p=1}^{N_P} U_{\ell,p} \quad (\text{F1})$$

with

$$U_{\ell,p} = \exp\left[-i \frac{\tau_\ell}{N_P} \mathcal{H}^{(\ell,p)}\right] \quad \text{and} \quad \mathcal{H}^{(\ell,p)} \equiv \mathcal{H}_0 + u^{(\ell,p)} \mathcal{H}_c. \quad (\text{F2})$$

and introduce the perturbed parameters

$$\tau'_\ell = \tau_\ell + \delta\tau_\ell, \quad u^{(\ell,p)'} = u^{(\ell,p)} + \delta u^{(\ell,p)} \quad (\text{F3})$$

Now, let us define the perturbed propagators

$$U'_{\ell,p} = \exp\left[-i \frac{\tau'_\ell}{N_P} (\mathcal{H}_0 + u^{(\ell,p)'} \mathcal{H}_c)\right]. \quad (\text{F4})$$

For small perturbations, we can write

$$\Delta U_{\ell,p} \equiv U'_{\ell,p} - U_{\ell,p} \approx \frac{\partial U_{\ell,p}}{\partial \tau_\ell} \delta\tau_\ell + \frac{\partial U_{\ell,p}}{\partial u^{(\ell,p)}} \delta u^{(\ell,p)}. \quad (\text{F5})$$

For the total propagator $U_{R,T}$ in Eq. (F1), we obtain for the average Hilbert-Schmidt norm of the deviation

$$\begin{aligned} & \mathbb{E} \|\Delta U_{\ell,p}\|_{HS} \quad (\text{F6}) \\ & \leq \sqrt{\frac{2}{\pi}} \left[\frac{\sigma_\tau}{N_P} \sum_{\ell=1}^{N_L} \sum_{p=1}^{N_P} \|\mathcal{H}^{(\ell,p)}\|_{HS} + \frac{\sigma_u}{N_P} \|\mathcal{H}_c\|_{HS} \sum_{\ell=1}^{N_L} \tau_\ell \right], \end{aligned}$$

where we assumed Gaussian-distributed perturbations of τ_ℓ with standard deviation σ_τ and of $u^{(\ell,p)}$ standard deviation σ_u . The same expression applies to the GRAPE propagator when $N_P = 1$.

Let us now turn to the state-transfer infidelity (10) and define the state-transfer infidelity for a unitary $U'_{\ell,p}$ as

$$J_s(U'_{\ell,p}) = 1 - |\langle \psi_T | U'_{\ell,p} | \psi_0 \rangle|^2, \quad (\text{F7})$$

where $|\psi_0\rangle$ is the initial state and $|\psi_T\rangle$ the target state. Assuming that $J_s(U_{\ell,p}) = 0$, i.e., the optimization found the optimal solution very accurately, the change in infidelity is

$$\Delta J_s \equiv J_s(U'_{\ell,p}) - J_s(U_{\ell,p}) = J_s(U'_{\ell,p}). \quad (\text{F8})$$

Writing $U'_{\ell,p} = U_{\ell,p} + \Delta U_{\ell,p}$ and expanding to first order in $\Delta U_{\ell,p}$, one finds

$$|\Delta J_s| \lesssim 2 |\langle \psi_0 | U_{\ell,p}^\dagger \Delta U_{\ell,p} | \psi_0 \rangle| \leq 2 \|\Delta U_{\ell,p}\|_{HS}. \quad (\text{F9})$$

This implies that $\mathbb{E} \|\Delta U_{\ell,p}\|_{HS}$ in Eq. (F6) bounds the change of the state-transfer infidelity from above.

We validate the perturbative bound with numerical simulations of the state-transfer problem on the 6-spin Ising spin chain of Sec. IV using both GRAPE and RALLY_T. For each pair of standard deviations (σ_u, σ_τ) ,

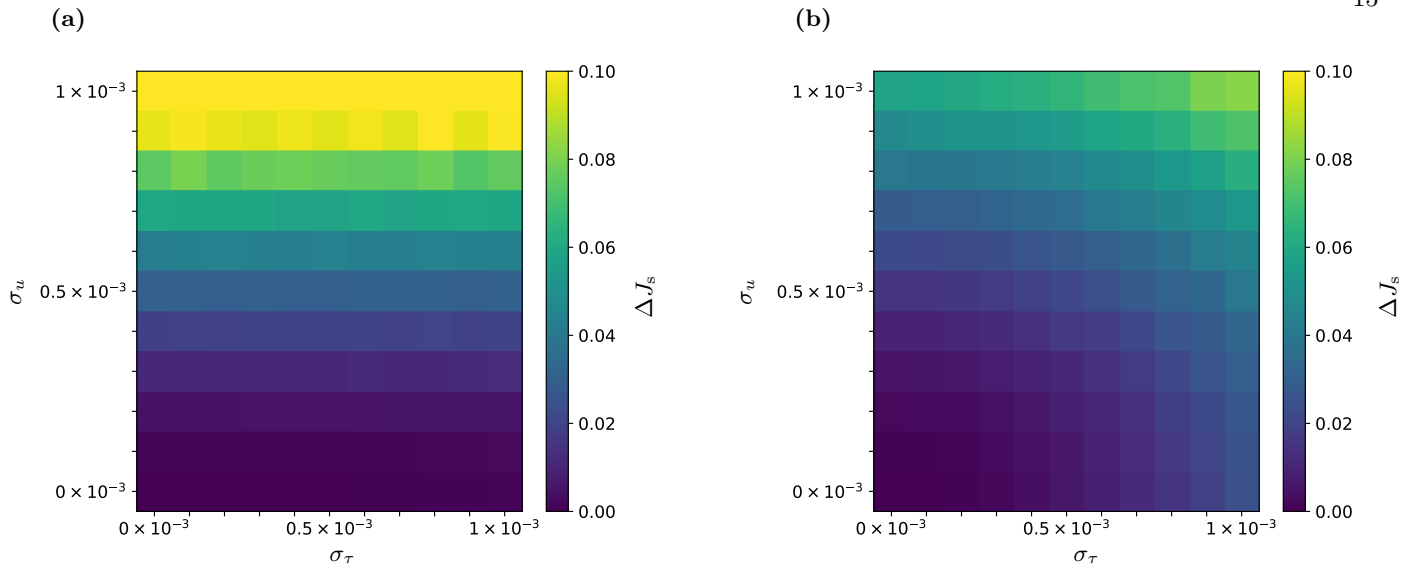


FIG. 10. Mean change in state-transfer infidelity ΔJ_s for GRAPE (a) and RALLY_T (b) on a 6-spin Ising chain under Gaussian uncertainties in control amplitudes $\delta u^{(\ell,p)}$ and pulse durations $\delta \tau_\ell$. Each point is averaged over 10 Gaussian perturbations for each of the 10 different random values of h_{ix} and h_{iz} . When compared to GRAPE's solutions, the solutions of RALLY_T appear more robust to deviations of the pulse amplitudes but less robust to deviations of the time durations due to the layer size $N_P > 1$.

we generate set of 10 different values of h_{ix} and h_{iz} , optimize the pulse sequences with GRAPE and RALLY_T to minimize J_s and then add independent Gaussian perturbations to every pulse ($\delta u^{(\ell,p)} \sim \mathcal{N}(0, \sigma_u)$) and $\delta \tau_\ell \sim \mathcal{N}(0, \sigma_\tau)$ with $\mathcal{N}(0, \sigma)$ being a Gaussian distribution with mean 0 and standard deviation σ). We obtain ΔJ_s and average it over 10 different perturbations for each of the 10 values of h_{ix} and h_{iz} . The results are shown in Fig. 10.

In RALLY_T, the contribution of the control-amplitude uncertainty to $\mathbb{E}\|\Delta U_{\ell,p}\|_{HS}$ (last term in Eq. (F6)) depends only on the total pulse-sequence time duration $\sum_{\ell=1}^{N_L} \tau_\ell$, but not on the total number of pulses $N_L N_P$. Thus, GRAPE and RALLY_T with similar total pulse-sequence time are expected to behave similarly with respect to amplitude uncertainty independent of the layer size N_P . This is confirmed by the results shown in Fig. 10, where RALLY_T solutions indicate a slightly higher robustness than GRAPE's solutions to deviations in the pulse amplitudes. In contrast, the contribution of the time uncertainty to $\mathbb{E}\|\Delta U_{\ell,p}\|_{HS}$ (first term in Eq. (F6)) is proportional to the total number of pulses $N_L N_P$. Thus, the robustness of the RALLY_T solutions is expected to be reduced by the factor $N_P > 1$, which is confirmed by the results shown in Fig. 10.

Appendix G: Experimental constraints for the globally-driven Rydberg platform

For the numerical simulations of a globally-driven Rydberg platform in Sec. IV, we use the real physical constraints of the PASQAL machine operating with Rubidium atoms [61]. These constraints are detailed in Table I.

Parameter	Value
Rydberg level n	70
Minimum Rabi frequency Ω_{\min}	0 MHz
Maximum Rabi frequency Ω_{\max}	10 MHz
Minimum Detuning Δ_{\min}	-10 MHz
Maximum Detuning Δ_{\max}	10 MHz
Minimum distance between atoms	5 μm
Minimum pulse duration	4 ns
Maximum pulse duration	$10^5 \mu\text{s}$
Interaction coefficient $C_{6,rr}$	5420 GHz μm^6

TABLE I. Physical constraints of the PASQAL machine operating with Rubidium atoms [61] considered in this article.

Appendix H: Details of unitary-synthesis optimization

We choose a non-symmetric spatial atom configuration for the unitary-synthesis problem. The positions of the atoms are (in μm)

$$\mathbf{r}_{q_0} = (-8, 0), \mathbf{r}_{q_1} = (0, 9.6), \mathbf{r}_{q_2} = (8.8, 0). \quad (\text{H1})$$

a. dCRAB settings: We use the QuOCS open-source optimal control suite [75] for the dCRAB simulations with the adaptive Nelder-Mead algorithm [50]. The number of super-iterations is 3 and the detuning is restricted to $\Delta \in [-10, 10]$ MHz by setting bounds in the optimization. The final evolution time T is 500 μs and the bandwidth limitation is $\Delta\Omega = 100/T$ to ensure successful optimization. All optimizer settings are summarized in Table II.

b. RALLY settings: The layer size is $N_P = 5$ and the detuning amplitude is restricted to

$\Delta \in [-10, 10]$ MHz. To ensure that these constraints are satisfied during RALLY_A optimizations, we enforce $\xi \in [0, 1]^{N_L}$. For RALLY_T, the minimum duration is set to 4 ns for every pulse in the optimization and the initial layer durations are chosen from a uniform distribution in $[0, 1]$ μ s. Optimization is performed with the Nelder–Mead method using the same settings as for the dCRAB algorithm.

Parameter	dCRAB	RALLY _T	RALLY _A
Structure	3 super-iter.	$N_P = 5$	$N_P = 5$
Detuning bounds	[-10, 10] MHz		
Final evolution time T	500 μ s	—	500 μ s
Bandwidth limit $\Delta\Omega$	100/ T	—	—
<code>xatol</code>		10^{-8}	
<code>fato1</code>		10^{-8}	
Optimizer	adaptive Nelder–Mead		
Max FoM evaluations		10^6	

TABLE II. Optimization settings for dCRAB and RALLY optimizations. Centered entries (spanning all method columns) denote parameters shared by all methods.

Appendix I: Rydberg-atom spatial configurations for the ground-state preparation and the corresponding target Hamiltonians

The choice of spatial configuration for the Rydberg atoms is crucial because a configuration that reflects the symmetry of the target Hamiltonian can constrain the optimization problem to a symmetry sector, thereby reducing the dimensionality of the relevant Hilbert subspace and easing the optimization. At the same time, symmetries of the spatial configuration beyond those of the Hamiltonian can prohibit the reachability of the target state [34].

1. Details of the optimization for the H₂ molecule

To describe the spin-orbital degrees of freedom for the H₂ molecule with an interatomic distance of 2 Ångström, we use the following target Hamiltonian

$$\begin{aligned}
\mathcal{H}_T = & -0.81054798 \mathbb{1} + 0.17218393 \sigma_0^z \\
& -0.22575349 \sigma_1^z + 0.17218393 \sigma_2^z \\
& -0.22575349 \sigma_3^z + 0.12091263 \sigma_1^z \sigma_0^z \\
& + 0.16892754 \sigma_2^z \sigma_0^z + 0.16614543 \sigma_2^z \sigma_1^z \\
& + 0.16614543 \sigma_3^z \sigma_0^z + 0.17464343 \sigma_3^z \sigma_1^z \\
& + 0.12091263 \sigma_3^z \sigma_2^z + 0.04523280 \sigma_3^x \sigma_2^x \sigma_1^x \sigma_0^x \\
& + 0.04523280 \sigma_3^x \sigma_2^x \sigma_1^y \sigma_0^y + 0.04523280 \sigma_3^y \sigma_2^y \sigma_1^x \sigma_0^x \\
& + 0.04523280 \sigma_3^y \sigma_2^y \sigma_1^y \sigma_0^y,
\end{aligned} \tag{I1}$$

which is obtained by using the Jordan-Wigner transformation.

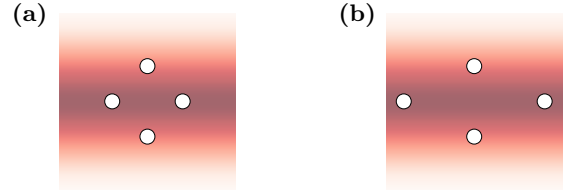


FIG. 11. Possible spatial configuration of Rydberg atoms in the simulator for the ground-state preparation of H₂ molecule. (a) The ring configuration introduces an additional symmetry of cyclic permutation not respected by the ground state of H₂. (b) The rhombic shape reflects the exchange symmetry of the target Hamiltonian. The atomic coordinates for this configuration, ordered by spin index (in μ m), are: (14, 0), (0, 7), (-14, 0), (0, -7).

Because of the Jordan-Wigner transformation used, the above Hamiltonian exhibits the symmetry of the simultaneous exchange of spins $0 \leftrightarrow 2$ and $1 \leftrightarrow 3$. Hence, we arrange the atoms on a rhombus, cf. Fig. 11, that respects this symmetry, thereby allowing the initial state $|\psi_0\rangle$ and the corresponding ground state to belong to a fully controllable symmetry sector of $N = 9$ dimensions described by $2N - 2 = 16$ real parameters. In contrast, a symmetric ring configuration would introduce the additional symmetry of cyclic permutation of the spins which is incompatible with the Hamiltonian, thereby preventing the reachability of the H₂ ground state [34].

For the optimization, we used the same setting as for the unitary-synthesis problem except that we limited the maximum number of figure-of-merit evaluations to $\leq 10^5$ for all methods. For RALLY_A, we set the final evolution time to $T = 100$ μ s. For dCRAB, a further bandwidth limit of $\Delta\Omega = 30/T$ was chosen.

2. Details of the optimization for the NO₃ molecule

To describe the NO₃ molecule with the spatial coordinates of the individual atoms given in Table III, we use a target spin Hamiltonian provided in Ref. [69]. Since parity encoding [76] was used, the 4-qubit Hamiltonian does not exhibit any symmetries related to the exchange of spins. Hence, a non-symmetric Rydberg-atom configuration, cf. Fig. 12, was chosen to obtain full controllability in the full Hilbert space of dimension $N = 16$ described by $2N - 2 = 30$ real parameters.

Atom	X	Y	Z
N	-0.0225	-0.0483	0.0029
O	-0.6411	1.0149	-0.0004
O	-0.6284	-1.1191	0.0095
O	1.2096	-0.0414	-0.0004

TABLE III. Spatial coordinates of atoms of the NO₃ molecule in Ångström used in our calculations.

For the optimization, we retained the parameters used for the unitary-synthesis problem. The only change was that, for dCRAB, the total evolution time was set to $T = 500 \mu\text{s}$ or $T = 3000 \mu\text{s}$ and the bandwidth was limited to $\Delta\Omega = 80/T$. For RALLY_A we used $T = 500 \mu\text{s}$.

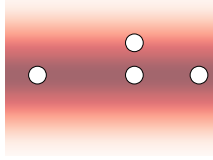


FIG. 12. Spatial configuration of Rydberg atoms used for the ground-state preparation of the NO₃ molecule. The atomic coordinates for this configuration, ordered by spin index (in μm) are: (10, 0), (0, 20), (0, 0), (0, -30).

3. Details of the optimization for the CH molecule

To describe the CH molecule with the spatial coordinates of the individual atoms given in Table IV, we use the target Hamiltonian provided in Ref. [69].

Atom	X Coordinate	Y Coordinate	Z Coordinate
C	0.0000	0.0000	-0.00198
H	0.0000	0.0000	1.1219

TABLE IV. Coordinates of atoms of the CH molecule used in our calculation (in Ångström).

Since the Jordan-Wigner transformation was used to obtain the 6-qubit target Hamiltonian, which induces a permutation symmetry of the qubits described above, one could think of choosing a spatial configuration of Rydberg atoms similar to the one shown in Fig. 11(b), for example the spatial configuration shown in Fig. 13(a). For this spatial configuration of the Rydberg atoms, we observe that the initial state $|\bar{0}\rangle$ is in a different symmetry sector compared to the ground state of CH. Therefore, we use the non-symmetric Rydberg-atom configuration shown in Fig. 13(b).

For the optimization, we used the same settings as for the unitary-synthesis case. The maximum number of figure-of-merit evaluations is limited to $\leq 1.5 \times 10^6$ for all methods. For dCRAB, we set the final evolution time to $T = 2000 \mu\text{s}$ and the bandwidth limit to $\Delta\Omega = 200/T$. For RALLY_A, we also use $T = 2000 \mu\text{s}$.

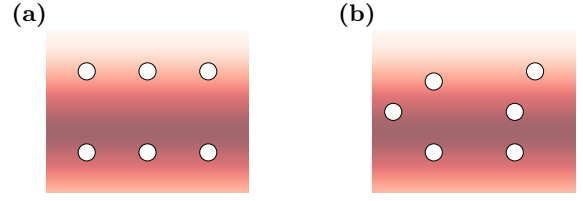


FIG. 13. Spatial configurations of Rydberg atoms in the simulator for the ground-state preparation of the CH molecule. (a) A symmetric configuration that cannot be used because the initial state $|\bar{0}\rangle$ belongs to a different symmetry sector than the ground state of the CH molecule. (b) This non-symmetric configuration allows us to reach the ground state of CH. The atomic coordinates for this configuration, ordered by spin index (in μm) are: (0, -12), (12, -24), (21, -12), (0, 12), (12, 12), (24, 18).

Appendix J: Von-Neumann entropy of the ground states of the molecules

We quantify entanglement by calculating the von-Neumann entropy S of the reduced density matrix of a single qubit and averaging S over all qubits. Table V shows the obtained von-Neumann entropies S along with the corresponding symmetry-sector dimensions. The ground states of NO₃ and CH exhibit significant higher entanglement than the ground state of H₂. The von-Neumann entropy was determined by means of the exact diagonalization of the Hamiltonian operators.

	H ₂	NO ₃	CH
dim	9	16	64
S	0.096	0.818	0.352

TABLE V. Entanglement S and relevant symmetry sector dimension dim of the three molecules analyzed.

Appendix K: Calculation of gradients for RALLY_T

To calculate the gradient of a figure of merit for the RALLY_T method, an analytical expression for the derivative $\partial U_{\text{R,T}}/\partial\tau_L$ is required. Let us first introduce the following notation

$$U^{(\ell,p)} = \exp\left(-i \frac{\tau_\ell}{N_{\text{P}}} \mathcal{H}^{(\ell,p)}\right), \quad U_{\text{R,T}} = \prod_{\ell=1}^{N_{\text{L}}} \prod_{p=1}^{N_{\text{P}}} U^{(\ell,p)}, \quad (\text{K1})$$

$$U_{<L} = \prod_{\ell=1}^{L-1} \prod_{p=1}^{N_{\text{P}}} U^{(\ell,p)}, \quad U_{>L} = \prod_{\ell=L+1}^{N_{\text{L}}} \prod_{p=1}^{N_{\text{P}}} U^{(\ell,p)}, \quad (\text{K2})$$

$$U_L^{(<r)} = \prod_{p=1}^{r-1} U^{(L,p)}, \quad U_L^{(\geq r)} = \prod_{p=r}^{N_P} U^{(L,p)}, \quad (\text{K3})$$

where $\mathcal{H}^{(\ell,p)}$ is defined in Eq. (F2). Using this notation, the derivative reads

$$\frac{\partial U_{\text{R,T}}}{\partial \tau_L} = U_{<L} \left[\sum_{r=1}^{N_P} \frac{(-i)}{N_P} U_L^{(<r)} \mathcal{H}^{(L,r)} U_L^{(\geq r)} \right] U_{>L}, \quad (\text{K4})$$

where we used that all pulses in a layer have the same time duration.

Appendix L: Calculation of gradients for GRAPE

For the GRAPE algorithm, computing the gradient of the unitary propagator with respect to the control amplitudes generally requires the Fréchet derivative of the matrix exponential. For time step j with piecewise-constant control $u(j)$, the Hamiltonian reads

$$\mathcal{H}_j \equiv \mathcal{H}_0 + u(j) \mathcal{H}_c, \quad (\text{L1})$$

and the corresponding propagator is

$$U_j \equiv U_j(\Delta t) = \exp(-i\Delta t \mathcal{H}_j). \quad (\text{L2})$$

A small perturbation $u(j) \rightarrow u(j) + \delta u(j)$ induces, to first order,

$$\delta U_j = -i\Delta t \delta u(j) \overline{\mathcal{H}_c} U_j, \quad (\text{L3})$$

$$\overline{\mathcal{H}_c} \Delta t = \int_0^{\Delta t} U_j(\tau) \mathcal{H}_c U_j(-\tau) d\tau, \quad (\text{L4})$$

which follows from Duhamel's formula

$$\left. \frac{d}{dx} e^{A+xB} \right|_{x=0} = \int_0^1 e^{(1-s)A} B e^{sA} ds. \quad (\text{L5})$$

For sufficiently small time steps ($\Delta t \ll \|\mathcal{H}_j\|^{-1}$), the relation $\overline{\mathcal{H}_c} \approx \mathcal{H}_c$ holds such that the gradient can be approximated using only matrix exponentials as

$$\delta U_j \approx -i\Delta t \delta u(j) \mathcal{H}_c U_j, \quad \text{i.e.,} \quad \frac{\partial U_j}{\partial u(j)} \approx -i\Delta t \mathcal{H}_c U_j. \quad (\text{L6})$$

However, approximating the Fréchet derivative yields inexact gradients which can alter the optimization trajectory and, most critically, the probability of success (the fraction of optimizations that reach the target fidelity). We observe this effect in our Ising-chain case study.

Moreover, many control problems exhibit a minimum evolution time T_{\min} below which high-fidelity solutions are unattainable; T_{\min} often increases with the Hilbert-space dimension N [44, 45, 77]. For the Ising chain, we

empirically find $T_{\min} \propto N = 2^n$. This has direct implications for GRAPE discretization. Let P be the number of optimization parameters, and $\Delta t = T/P$ the pulse-time discretization. Then, when working with a number of parameters close to the lower bound, $P \gtrsim 2N - 2$, the discretization does not become finer; consequently, the small- Δt approximation does not improve as the dimensionality of the problem increases.

Appendix M: Calculation of gradients for RALLY_A

For the propagator of RALLY_A in Eq. (3), we introduce the pulse Hamiltonian and the propagator for completeness

$$\mathcal{H}^{(\ell,p)}(\xi_\ell) = \mathcal{H}_0 + \xi_\ell u^{(\ell,p)} \mathcal{H}_c, \quad (\text{M1})$$

$$U^{(\ell,p)}(\xi_\ell) = \exp \left[-i\Delta t \mathcal{H}^{(\ell,p)}(\xi_\ell) \right] \quad (\text{M2})$$

so that

$$U_{\text{R,A}}(\xi) = \prod_{\ell=1}^{N_L} \prod_{p=1}^{N_P} U^{(\ell,p)}(\xi_\ell). \quad (\text{M3})$$

Using the same notation as in Sec. K, the exact derivative with respect to the layer amplitude ξ_L is

$$\frac{\partial U_{\text{R,A}}}{\partial \xi_L} = U_{<L} \left[\sum_{r=1}^{N_P} (-i\Delta t u^{(L,r)}) U_L^{(<r)} \overline{\mathcal{H}_c}^{(L,r)} U_L^{(\geq r)} \right] U_{>L}. \quad (\text{M4})$$

where $\overline{\mathcal{H}_c}^{(L,r)}$ is the Duhamel (Fréchet) integral of the control Hamiltonian

$$\overline{\mathcal{H}_c}^{(L,r)} \Delta t = \int_0^{\Delta t} U^{(L,r)}(\tau) \mathcal{H}_c U^{(L,r)}(-\tau) d\tau \quad (\text{M5})$$

and

$$U^{(L,r)}(\tau) = \exp[-i\tau \mathcal{H}^{(L,r)}(\xi_L)]. \quad (\text{M6})$$

Appendix N: Theoretical expectations for the runtime scaling of RALLY_T and GRAPE

For the GRAPE algorithm, a single gradient evaluation is based on the Fréchet derivative of the matrix exponential, which can be obtained from matrix diagonalization which exhibits a $\mathcal{O}(N^3)$ scaling (see Appendix L for details). For a control field, at least $2N - 2$ time bins (optimization parameters) are required for ground-state preparation and state-transfer problems and, hence, one optimization iteration of GRAPE involves $2N - 2$ diagonalizations. For n_{it} optimization iterations, this yields for the runtime scaling

$$\mathcal{C}_{\text{GRAPE}} = \mathcal{O}(n_{\text{it}} N^4). \quad (\text{N1})$$

Note that one can avoid calculating the full Fréchet matrix by directly using Krylov-subspace methods, which

typically reduces the runtime scaling to $\mathcal{O}(n_{\text{it}}N^3)$. However, for the system sizes considered in the main text, using the Krylov-subspace method resulted in an overall slower calculation and, therefore, full diagonalization was used.

In the RALLY_T method, diagonalization is performed only once before the optimization, for example for the two static Hamiltonians associated with the control values $J = \pm 1$ in Sec. IV C. This pre-diagonalization exhibits an $\mathcal{O}(N^3)$ scaling of the runtime. For the optimization, each evaluation of the figure of merit and its gradient involves $N_{\text{P}}N_{\text{L}}$ matrix–vector multiplications. For $N_{\text{L}} \approx 2N - 2$ and a fixed layer size N_{P} , the scaling for n_{it} iterations hence reads

$$\mathcal{C}_{\text{RALLY}_T} = \underbrace{\mathcal{O}(N^3)}_{\text{pre-diagonalization}} + \underbrace{\mathcal{O}(n_{\text{it}} N^3)}_{\text{per-iteration cost}}, \quad (\text{N2})$$

where the second term usually dominates. Comparing Eqs. (N1) and (N2) implies that the RALLY_T method exhibits a more favourable scaling than GRAPE for the system sizes considered. From practical calculations, we observe that the number of iterations n_{it} necessary for finding the solution scales approximately as $n_{\text{it}} = \mathcal{O}(N^{1/2})$ for both RALLY methods and GRAPE.

Appendix O: Finite-bandwidth interpolation between control pulses

To account for finite control bandwidth in experimental settings, we introduce a smooth interpolation for each discontinuous jump between the constant-amplitude pulses in the RALLY_T propagator $U_{\text{R},T}$. When the control is changed from the starting pulse amplitude u_0 to the final pulse amplitude u_1 over a time interval $[t_0, t_1]$ of duration $\tau_{\text{rise}} = t_1 - t_0$, we use the interpolation $f_{\text{int}}(t) = u_0 + (u_1 - u_0)s(t)$ with $t \in [t_0, t_1]$ and the shifted

sigmoid function

$$s(t) = \frac{1}{2} \left[1 + \tanh \left(\frac{k}{2} (t - t_{\text{m}}) \right) \right], \quad (\text{O1})$$

where

$$k = \frac{2}{\tau_{\text{rise}}} \ln \left(\frac{1 - \varepsilon}{\varepsilon} \right), \quad t_{\text{m}} = \frac{t_0 + t_1}{2}. \quad (\text{O2})$$

The time τ_{rise} determines the duration of the transition centered at t_{m} , while ε controls the shape. The steepness k is fixed by τ_{rise} and ε so that $f_{\text{int}}(t_{\text{m}} \pm \tau_{\text{rise}}/2)$ is ε away from u_1 and u_0 , respectively.

For the numerical simulations, we divide $[t_0, t_1]$ into N_{int} equal intervals of length $\Delta t = \tau_{\text{rise}}/N_{\text{int}}$ and approximate the continuous interpolation by a product of short-time propagators with constant Hamiltonian in these intervals. We define $u_n = f_{\text{int}}(t_n)$ for $t_n = t_0 + (n - 1/2)\Delta t$ and $n = 1, \dots, N_{\text{int}}$. Using $\mathcal{H}(u_n) = \mathcal{H}_0 + u_n \mathcal{H}_c$, the unitary propagator associated with a single interpolation reads

$$U_{\text{rise}}(u_0 \rightarrow u_1) = \prod_{n=1}^{N_{\text{int}}} \exp \left[-i \Delta t \mathcal{H}(u_n) \right]. \quad (\text{O3})$$

In the RALLY_T propagator $U_{\text{R},T}$, an interpolation propagator U_{rise} is inserted between each pair of constant-amplitude pulses, so that each instantaneous jump $u_0 \rightarrow u_1$ is replaced by a finite-time ramp. This yields a pulse sequence with finite-bandwidth pulses. Importantly, these interpolation propagators can be prepared prior to the optimization for RALLY_T, because the pulse amplitudes are randomly chosen in advance and the interpolation does not depend on the pulse durations which are varied. This reduces the computational overhead for including finite control bandwidth in the optimization significantly.

For the specific optimization problem studied in Sec. IV C, we chose $\tau_{\text{rise}} = 10$, $N_{\text{int}} = 100$ and $\varepsilon = 10^{-10}$ for each interpolation propagator.

-
- [1] S. J. Glaser, U. Boscain, T. Calarco, C. P. Koch, W. Köckenberger, R. Kosloff, I. Kuprov, B. Luy, S. Schirmer, T. Schulte-Herbrüggen, D. Sugny, and F. K. Wilhelm, Training schrödinger’s cat: quantum optimal control, *The European Physical Journal D* **69**, 279 (2015).
- [2] C. P. Koch, U. Boscain, T. Calarco, G. Dirr, S. Filipp, S. J. Glaser, R. Kosloff, S. Montangero, T. Schulte-Herbrüggen, D. Sugny, and F. K. Wilhelm, Quantum optimal control in quantum technologies. strategic report on current status, visions and goals for research in europe, *EPJ Quantum Technology* **9**, 19 (2022).
- [3] Q. Ansel, E. Dionis, F. Arrouas, B. Peaudecerf, S. Guérin, D. Guéry-Odelin, and D. Sugny, Introduction to theoretical and experimental aspects of quantum optimal control, *Journal of Physics B: Atomic, Molecular and Optical Physics* **57**, 133001 (2024).
- [4] O. V. Morzhin and A. N. Pechen, Krotov method for optimal control of closed quantum systems, *Russian Math. Surveys* **74**, 851 (2019).
- [5] N. Khaneja, T. Reiss, C. Kehlet, T. Schulte-Herbrüggen, and S. J. Glaser, Optimal control of coupled spin dynamics: design of nmr pulse sequences by gradient ascent algorithms, *Journal of Magnetic Resonance* **172**, 296 (2005).
- [6] T. Caneva, T. Calarco, and S. Montangero, Chopped random-basis quantum optimization, *Phys. Rev. A* **84**, 022326 (2011).
- [7] N. Rach, M. M. Müller, T. Calarco, and S. Montangero, Dressing the chopped-random-basis optimization

- tion: A bandwidth-limited access to the trap-free landscape, *Phys. Rev. A* **92**, 062343 (2015).
- [8] S. Machnes, E. Assémat, D. Tannor, and F. K. Wilhelm, Tunable, flexible, and efficient optimization of control pulses for practical qubits, *Phys. Rev. Lett.* **120**, 150401 (2018).
- [9] F. Schäfer, P. Sekatski, M. Koppenhöfer, C. Bruder, and M. Kloc, Control of stochastic quantum dynamics by differentiable programming, *Machine Learning: Science and Technology* **2**, 035004 (2021).
- [10] V. V. Sivak, A. Eickbusch, H. Liu, B. Royer, I. Tsioutsios, and M. H. Devoret, Model-free quantum control with reinforcement learning, *Phys. Rev. X* **12**, 011059 (2022).
- [11] D. J. Egger and F. K. Wilhelm, Adaptive hybrid optimal quantum control for imprecisely characterized systems, *Phys. Rev. Lett.* **112**, 240503 (2014).
- [12] J. Kelly, R. Barends, B. Campbell, Y. Chen, Z. Chen, B. Chiaro, A. Dunsworth, A. G. Fowler, I.-C. Hoi, E. Jeffrey, A. Megrant, J. Mutus, C. Neill, P. J. J. O’Malley, C. Quintana, P. Roushan, D. Sank, A. Vainsencher, J. Wenner, T. C. White, A. N. Cleland, and J. M. Martinis, Optimal quantum control using randomized benchmarking, *Phys. Rev. Lett.* **112**, 240504 (2014).
- [13] H. Rabitz, R. de Vivie-Riedle, M. Motzkus, and K. Kompa, Whither the future of controlling quantum phenomena?, *Science* **288**, 824 (2000).
- [14] A. Marshall, T. Reisser, P. Rembold, C. Müller, J. Scheuer, M. Gierse, T. Eichhorn, J. M. Steiner, P. Hautle, T. Calarco, F. Jelezko, M. B. Plenio, S. Montangero, I. Schwartz, M. M. Müller, and P. Neumann, Macroscopic hyperpolarization enhanced with quantum optimal control, *Phys. Rev. Res.* **4**, 043179 (2022).
- [15] S. Rosi, A. Bernard, N. Fabbri, L. Fallani, C. Fort, M. Inguscio, T. Calarco, and S. Montangero, Fast closed-loop optimal control of ultracold atoms in an optical lattice, *Phys. Rev. A* **88**, 021601 (2013).
- [16] P. Doria, T. Calarco, and S. Montangero, Optimal control technique for many-body quantum dynamics, *Phys. Rev. Lett.* **106**, 190501 (2011).
- [17] F. Dolde, V. Bergholm, Y. Wang, I. Jakobi, B. Naydenov, S. Pezzagna, J. Meijer, F. Jelezko, P. Neumann, T. Schulte-Herbrüggen, J. Biamonte, and J. Wrachtrup, High-fidelity spin entanglement using optimal control, *Nature Communications* **5**, 3371 (2014).
- [18] G. Waldherr, Y. Wang, S. Zaiser, M. Jamali, T. Schulte-Herbrüggen, H. Abe, T. Ohshima, J. Isoya, J. F. Du, P. Neumann, and J. Wrachtrup, Quantum error correction in a solid-state hybrid spin register, *Nature* **506**, 204 (2014).
- [19] P. Rembold, N. Oshnik, M. M. Müller, S. Montangero, T. Calarco, and E. Neu, Introduction to quantum optimal control for quantum sensing with nitrogen-vacancy centers in diamond, *AVS Quantum Science* **2**, 024701 (2020).
- [20] A. Omran, H. Levine, A. Keesling, G. Semeghini, T. T. Wang, S. Ebadi, H. Bernien, A. S. Zibrov, H. Pichler, S. Choi, J. Cui, M. Rossignolo, P. Rembold, S. Montangero, T. Calarco, M. Endres, M. Greiner, V. Vuletić, and M. D. Lukin, Generation and manipulation of schrödinger cat states in rydberg atom arrays, *Science* **365**, 570 (2019).
- [21] C. Kokail, C. Maier, R. van Bijnen, T. Brydges, M. K. Joshi, P. Jurcevic, C. A. Muschik, P. Silvi, R. Blatt, C. F. Roos, and P. Zoller, Self-verifying variational quantum simulation of lattice models, *Nature* **569**, 355–360 (2019).
- [22] U. Boscain, M. Sigalotti, and D. Sugny, Introduction to the pontryagin maximum principle for quantum optimal control, *PRX Quantum* **2**, 030203 (2021).
- [23] G. Dridi, M. Lapert, J. Salomon, S. J. Glaser, and D. Sugny, Discrete-valued-pulse optimal control algorithms: Application to spin systems, *Phys. Rev. A* **92**, 043417 (2015).
- [24] D. Suter and G. A. Álvarez, Colloquium: Protecting quantum information against environmental noise, *Rev. Mod. Phys.* **88**, 041001 (2016).
- [25] L. Viola and S. Lloyd, Dynamical suppression of decoherence in two-state quantum systems, *Phys. Rev. A* **58**, 2733 (1998).
- [26] N. Khaneja, R. Brockett, and S. J. Glaser, Time optimal control in spin systems, *Phys. Rev. A* **63**, 032308 (2001).
- [27] U. Boscain and P. Mason, Time minimal trajectories for a spin 1/2 particle in a magnetic field, *Journal of Mathematical Physics* **47**, 062101 (2006).
- [28] A. Pagano, M. M. Müller, T. Calarco, S. Montangero, and P. Rembold, Role of bases in quantum optimal control, *Phys. Rev. A* **110**, 062608 (2024).
- [29] J. Emerson, E. Livine, and S. Lloyd, Convergence conditions for random quantum circuits, *Phys. Rev. A* **72**, 060302 (2005).
- [30] K. W. Moore and H. Rabitz, Exploring constrained quantum control landscapes, *The Journal of Chemical Physics* **137**, 134113 (2012).
- [31] S. Lloyd and S. Montangero, Information theoretical analysis of quantum optimal control, *Phys. Rev. Lett.* **113**, 010502 (2014).
- [32] The results of this article are readily extended to the general case of many control fields $u_k(t)$ with corresponding control Hamiltonians \mathcal{H}_k such that the total Hamiltonian reads $\mathcal{H}(t) = \mathcal{H}_0 + \sum_k u_k(t)\mathcal{H}_k$.
- [33] D. D’Alessandro, *Introduction to Quantum Control and Dynamics*, Chapman & Hall/CRC Applied Mathematics & Nonlinear Science (CRC Press, 2007).
- [34] J. Singh, A. Kruckenhauser, R. van Bijnen, and R. Zeier, Ground-state reachability for variational quantum eigensolvers: a rydberg-atom case study (2025), [arXiv:2506.22387 \[quant-ph\]](https://arxiv.org/abs/2506.22387).
- [35] S. van Frank, M. Bonneau, J. Schmiedmayer, S. Hild, C. Gross, M. Cheneau, I. Bloch, T. Pichler, A. Negretti, T. Calarco, and S. Montangero, Optimal control of complex atomic quantum systems, *Scientific Reports* **6**, 34187 (2016).
- [36] T. Caneva, T. Calarco, R. Fazio, G. E. Santoro, and S. Montangero, Speeding up critical system dynamics through optimized evolution, *Phys. Rev. A* **84**, 012312 (2011).
- [37] S. Kirchhoff, T. Keßler, P. J. Liebermann, E. Assémat, S. Machnes, F. Motzoi, and F. K. Wilhelm, Optimized cross-resonance gate for coupled transmon systems, *Phys. Rev. A* **97**, 042348 (2018).
- [38] T. Caneva, M. Murphy, T. Calarco, R. Fazio, S. Montangero, V. Giovannetti, and G. E. Santoro, Optimal control at the quantum speed limit, *Phys. Rev. Lett.* **103**, 240501 (2009).
- [39] L. Mandelstam and I. Tamm, The uncertainty relation between energy and time in non-relativistic quantum mechanics, in *Selected Papers*, edited by B. M. Bolotovskii, V. Y. Frenkel, and R. Peierls (Springer Berlin Heidelberg, Berlin, Heidelberg, 1991) pp. 115–123.

- [40] J. Anandan and Y. Aharonov, Geometry of quantum evolution, *Phys. Rev. Lett.* **65**, 1697 (1990).
- [41] N. Margolus and L. B. Levitin, The maximum speed of dynamical evolution, *Physica D: Nonlinear Phenomena* **120**, 188–195 (1998).
- [42] S. Deffner and S. Campbell, Quantum speed limits: from heisenberg’s uncertainty principle to optimal quantum control, *Journal of Physics A: Mathematical and Theoretical* **50**, 453001 (2017).
- [43] A. Farmanian and V. Karimpour, Quantum speed limits for implementation of unitary transformations, *Phys. Rev. A* **110**, 042611 (2024).
- [44] M. Murphy, S. Montangero, V. Giovannetti, and T. Calarco, Communication at the quantum speed limit along a spin chain, *Phys. Rev. A* **82**, 022318 (2010).
- [45] M. Bukov, D. Sels, and A. Polkovnikov, Geometric speed limit of accessible many-body state preparation, *Phys. Rev. X* **9**, 011034 (2019).
- [46] P. M. Poggi, Geometric quantum speed limits and short-time accessibility to unitary operations, *Phys. Rev. A* **99**, 042116 (2019).
- [47] T. Caneva, A. Silva, R. Fazio, S. Lloyd, T. Calarco, and S. Montangero, Complexity of controlling quantum many-body dynamics, *Phys. Rev. A* **89**, 042322 (2014).
- [48] M. M. Müller, R. S. Said, F. Jelezko, T. Calarco, and S. Montangero, One decade of quantum optimal control in the chopped random basis, *Reports on Progress in Physics* **85**, 076001 (2022).
- [49] J. A. Nelder and R. Mead, A simplex method for function minimization, *Computer Journal* **7**, 308 (1965).
- [50] F. Gao and L. Han, Implementing the nelder-mead simplex algorithm with adaptive parameters, *Computational Optimization and Applications* **51**, 259 (2012).
- [51] R. Porotti, V. Peano, and F. Marquardt, Gradient-ascent pulse engineering with feedback, *PRX Quantum* **4**, 030305 (2023).
- [52] In general, the individual pulse durations within a layer could be chosen as arbitrary fractions of τ_e .
- [53] J. Gemmer and G. Mahler, Distribution of local entropy in the hilbert space of bi-partite quantum systems: origin of jaynes’ principle, *The European Physical Journal B - Condensed Matter and Complex Systems* **31**, 249 (2003).
- [54] S. Goldstein, J. L. Lebowitz, R. Tumulka, and N. Zanghì, Canonical typicality, *Phys. Rev. Lett.* **96**, 050403 (2006).
- [55] S. Popescu, A. J. Short, and A. Winter, Entanglement and the foundations of statistical mechanics, *Nature Physics* **2**, 754 (2006).
- [56] A. J. Scott, Optimizing quantum process tomography with unitary 2-designs, *Journal of Physics A: Mathematical and Theoretical* **41**, 055308 (2008).
- [57] A. Pagano, S. Weber, D. Jäschke, T. Pfau, F. Meinert, S. Montangero, and H. P. Büchler, Error budgeting for a controlled-phase gate with strontium-88 rydberg atoms, *Phys. Rev. Res.* **4**, 033019 (2022).
- [58] M. Morgado and S. Whitlock, Quantum simulation and computing with rydberg-interacting qubits, *AVS Quantum Science* **3**, 023501 (2021).
- [59] P. J. Vetter, T. Reisser, M. G. Hirsch, T. Calarco, F. Motzoi, F. Jelezko, and M. M. Müller, Gate-set evaluation metrics for closed-loop optimal control on nitrogen-vacancy center ensembles in diamond, *npj Quantum Information* **10**, 96 (2024).
- [60] A. Ketterer and T. Wellens, Characterizing crosstalk of superconducting transmon processors, *Phys. Rev. Appl.* **20**, 034065 (2023).
- [61] H. Silvério, S. Grijalva, C. Dalyac, L. Leclerc, P. J. Karalekas, N. Shammah, M. Beji, L.-P. Henry, and L. Henriot, Pulser: An open-source package for the design of pulse sequences in programmable neutral-atom arrays, *Quantum* **6**, 629 (2022).
- [62] To speed up the calculation, we used a gradient-based optimization (L-BFGS-B [72]) but gradient-free methods yield qualitatively similar results.
- [63] J. Tilly, H. Chen, S. Cao, D. Picozzi, K. Setia, Y. Li, E. Grant, L. Wossnig, I. Rungger, G. H. Booth, and J. Tennyson, The Variational Quantum Eigensolver: A review of methods and best practices, *Physics Reports* **986**, 1 (2022), arXiv:2111.05176 [quant-ph].
- [64] O. R. Meitei, B. T. Gard, G. S. Barron, D. P. Pappas, S. E. Economou, E. Barnes, and N. J. Mayhall, Gate-free state preparation for fast variational quantum eigensolver simulations, *npj Quantum Information* **7**, 155 (2021).
- [65] T. Caneva, T. Calarco, R. Fazio, G. E. Santoro, and S. Montangero, Speeding up critical system dynamics through optimized evolution, *Physical Review A* **84**, 10.1103/physreva.84.012312 (2011).
- [66] A. B. Magann, C. Arenz, M. D. Grace, T.-S. Ho, R. L. Kosut, J. R. McClean, H. A. Rabitz, and M. Sarovar, From pulses to circuits and back again: A quantum optimal control perspective on variational quantum algorithms, *PRX Quantum* **2**, 010101 (2021).
- [67] M. Suzuki, Generalized trotter’s formula and systematic approximants of exponential operators and inner derivations with applications to many-body problems, *Communications in Mathematical Physics* **51**, 183 (1976).
- [68] U. Schollwöck, The density-matrix renormalization group in the age of matrix product states, *Annals of Physics* **326**, 96 (2011).
- [69] <https://github.com/marcodallara/RALLY>.
- [70] F. Gago-Encinas, T. Hartung, D. M. Reich, K. Jansen, and C. P. Koch, Determining the ability for universal quantum computing: Testing controllability via dimensional expressivity, *Quantum* **7**, 1214 (2023).
- [71] M. R. Hestenes and E. Stiefel, Methods of conjugate gradients for solving linear systems, *Journal of research of the National Bureau of Standards* **49**, 409 (1952).
- [72] C. Zhu, R. H. Byrd, P. Lu, and J. Nocedal, Algorithm 778: L-bfgs-b: Fortran subroutines for large-scale bound-constrained optimization, *ACM Trans. Math. Softw.* **23**, 550–560 (1997).
- [73] A. O. Barut and R. Raczka, *A. O. Barut and R. Raczka: Theory of Group Representations and Applications* (World Scientific, Singapore, 1987).
- [74] B. Collins, Moments and cumulants of polynomial random variables on unitary groups, the itzykson-zuber integral, and free probability, *International Mathematics Research Notices* **2003**, 953 (2003).
- [75] M. Rossignolo, T. Reisser, A. Marshall, P. Rembold, A. Pagano, P. J. Vetter, R. S. Said, M. M. Müller, F. Motzoi, T. Calarco, F. Jelezko, and S. Montangero, QuOCS: The Quantum Optimal Control Suite, *Computer Physics Communications* , 108782 (2023).
- [76] J. T. Seeley, M. J. Richard, and P. J. Love, The bravyi-kitaev transformation for quantum computation of electronic structure, *The Journal of Chemical Physics* **137**, 224109 (2012).
- [77] M. Larocca and D. Wisniacki, Krylov-subspace approach for the efficient control of quantum many-body dynamics,

